AGU PUBLICATIONS

JGR

Journal of Geophysical Research: Solid Earth

RESEARCH ARTICLE
10.1002/2014JB011389

Key Points:
- We introduce a novel technique to determine NVT source locations and mechanisms
- Energy-based and particle motion polarization metrics to analyze tremors
- NVT locations and mechanisms in Guerrero are in agreement with those of LFEs

Supporting Information:
- Figures S1–S5

Correspondence to:
V. M. Cruz-Atienza,
cruz@geofisica.unam.mx

Citation:
Cruz-Atienza, V. M., A. Husker, D. Legrand, E. Caballero, and V. Kostoglodov (2015), Nonvolcanic tremor locations and mechanisms in Guerrero, Mexico, from energy-based and particle motion polarization analysis, *J. Geophys. Res. Solid Earth*, *120*, doi:10.1002/2014JB011389.

Received 15 JUN 2014
Accepted 26 NOV 2014
Accepted article online 4 DEC 2014

Nonvolcanic tremor locations and mechanisms in Guerrero, Mexico, from energy-based and particle motion polarization analysis

Víctor M. Cruz-Atienza[1], Allen Husker[1], Denis Legrand[1], Emmanuel Caballero[1], and Vladimir Kostoglodov[1]

[1]Instituto de Geofísica, Universidad Nacional Autónoma de México, Mexico City, Mexico

Abstract We introduce the Tremor Energy and Polarization (TREP) method, which jointly determines the source location and focal mechanism of sustained nonvolcanic tremor (NVT) signals. The method minimizes a compound cost function by means of a grid search over a three-dimensional hypocentral lattice. Inverted metrics are derived from three NVT observables: (1) the energy spatial distribution, (2) the energy spatial derivatives, and (3) the azimuthal direction of the particle motion polarization ellipsoid. To assess the tremor sources, TREP assumes double-couple point dislocations with frequency-dependent quality factors (Q) in a layered medium. Performance and resolution of the method is thoroughly assessed via synthetic inversion tests with random noise, where the "observed" data correspond to an NVT-like finite difference (FD) model we introduce. The FD tremor source is composed of hundreds of quasi-dynamic penny-shaped cracks governed by a time-weakening friction law. In agreement with previous works, epicentral locations of 26 NVTs in Guerrero are separated in two main groups, one between 200 and 230 km from the trench, and another at about 170 km. However, unlike earlier investigations, most NVT hypocenters concentrate at 43 km depth near the plate interface and have subparallel rake angles to the Cocos plate convergence direction. These locations have uncertainties of ~5 km in the three components and are consistent with independent results for low-frequency earthquakes in the region, supporting their common origin related to slip transients in the plate interface. Our results also suggest the occurrence of NVT sources within the slab, ~5 km below the interface.

1. Introduction

The discovery of nonvolcanic tremors (NVT) [*Obara*, 2002] and slow (or silent) slip events (SSE) [*Dragert et al*., 2001] has provided key elements to understand fault mechanics in deep subduction interfaces. In some regions, such as the Cascadia and Nankai subduction zones, these phenomena are usually correlated in space and time, with recurrence intervals from several months to years [e.g., *Rogers and Dragert*, 2003; *Obara et al*., 2004]. Low- (i.e., 1–5 Hz) and very low (i.e., 0.02–0.05 Hz) frequency earthquakes (LFE and VLF, respectively) with SSE-consistent focal mechanisms (i.e., shallow thrust faulting) have also been observed along the subduction interface of southwest Japan [*Shelly et al*., 2007; *Ito et al*., 2007], with the LFEs proposed as the elementary unit of sustained tremor signals (i.e., NVTs are the summation of LFEs) [*Shelly et al*., 2007; *Ide et al*., 2007]. Since LFE locations in different subduction regions are constrained near the interface of the plates [e.g., *Ide et al*., 2007; *Brown et al*., 2009; *Bostock et al*., 2012; *Frank et al*., 2013], this hypothesis assumes that the sources of NVT are also located close to the interface. However, tremor locations with an independent method in Cascadia [*Kao et al*., 2005, 2009] suggest that tremors are not originated at the plate interface where SSEs are supposed to occur. Recent observations of nonlinear crustal deformations during SSEs in Guerrero, Mexico, revealed transient reductions of the rocks resistance (i.e., the shear modulus) in the middle and lower crust [*Rivet et al*., 2011, 2013]. Therefore, this phenomenon represents a possible mechanism promoting shear failures in widespread regions around the silent slipping surface. LFEs are usually detected after stacking tiny signals to obtain higher correlation coefficients between waveforms [e.g., *Shelly et al*., 2006]. These are low-frequency signals embedded in a broader band long-duration record where a significant amount of energy corresponds to "incoherent" arrivals, namely, tremor bursts. In other terms, the band-limited seismic radiation whose source has been identified as shear failures near to the plate interface is only a fraction of the information recorded during tremor episodes. A comprehensive review of these phenomena may be found in *Beroza and Ide* [2011].

SSEs in Mexico were first reported [*Lowry et al*., 2001] the same year the phenomenon was discovered in Cascadia [*Dragert et al*., 2001]. Further investigations of silent earthquakes in Guerrero allowed the understanding of the spatial extent and propagation patterns of the transient slips at the plate interface [*Iglesias et al*., 2004; *Franco et al*., 2005; *Vergnolle et al*., 2010; *Radiguet et al*., 2012; *Cavalié et al*., 2013]. Unlike other subduction zones, NVT episodes in Guerrero are not always concomitant with large, long-term SSEs [*Payero et al*., 2008; *Husker et al*., 2012], suggesting that tremors and silent earthquakes may have different origins [*Kostoglodov et al*., 2010]. However, NVT bursts observed during inter-SSE periods may be possibly related to small, short-term slip transients with subcentimeter surface displacements [*Vergnolle et al*., 2010]. Detailed spatiotemporal tracking of the NVT and LFE activity with accurate estimates of the source depth and mechanism may provide key elements to better elucidate the relationship between both phenomena.

The largest difficulty to locate tremors is their emergent and sustained character, where almost no coherent phases can be visually identified. Most of the current methods to locate NVTs are based on cross-correlation measurements of waveform templates or envelopes [e.g., *Obara*, 2002; *Shelly et al*., 2006; *Ide et al*., 2007; *Payero et al*., 2008; *Wech and Creager*, 2008; *Brown et al*., 2009; *Obara*, 2010]. Time lags between the maximum cross-correlation coefficients are then used as travel times to locate the source. When dense seismic arrays are available, beam-forming analysis [*Ghosh et al*., 2009] and energy attenuation patterns [*Maeda and Obara*, 2009; *Kostoglodov et al*., 2010; *Husker et al*., 2012] may also be used, although these approaches lack of depth resolution so the source depth is usually fixed to analyze epicenter locations.

Evidence of NVT in widespread three-dimensional regions is based on source locations using two different methods: the source-scanning algorithm (SSA) [*Kao and Shan*, 2004; *Kao et al*., 2005, 2009] and the envelope cross-correlation method [*Obara*, 2002]. Envelope cross-correlation locations suffer from a lack of precise arrival time peaking due to long-duration envelopes used for this purpose (i.e., minutes long). Although improvements have been made to the method [e.g., *Obara et al*., 2010], this issue may translate as inaccurate depth estimates [e.g., *Payero et al*., 2008]. An interesting work to locate the source of tremor by combining the energy distribution and the envelope arrival times has been introduced by *Maeda and Obara* [2009]. However, no estimates of errors in depth are reported in the study. The other method, the SSA, is based on move-out summation of seismogram windows without considering the source radiation pattern, and so tremor depths may suffer from significant errors, as we shall discuss later. Thus, there are no convincing results about the depths where the sustained tremor bursts are generated. Reliable locations of these seismic events based on a robust and distinct method may help to further elucidate whether the hypothesis stating that LFEs represent the elementary unit of NVTs is plausible in the entire frequency band where the NVTs are observed.

NVT (and LFE) amplitudes and waveforms depend on both the source location and mechanism. Solving these source parameters by simultaneously explaining independent properties of the radiated wavefield may lead to robust location estimates. Previous works have demonstrated that the energy spatial distribution of the NVT records and the associated particle motion polarization are two source-dependent properties that are clearly observed in Guerrero and Cascadia [*Kostoglodov et al*., 2010; *Husker et al*., 2012; *Wech and Creager*, 2007]. In this study, we introduce a new technique that combines these properties to assess the source of sustained tremor signals.

2. NVT Location Technique

The location technique, called the "Tremor Energy and Polarization" (TREP) method, consists of a grid search over a three-dimensional hypocenter lattice to investigate the source location (i.e., the three hypocentral coordinates) and mechanism (i.e., the rake angle) that minimize a cost function involving different observables. A similar approach based on displacement amplitudes to determine the location and focal mechanism of volcanic sources was proposed by *Legrand et al*. [2000]. The observables used here, which are described in the next section, are translated into energy and particle motion polarization metrics that are simultaneously inverted to determine the source parameters mentioned above.

A three-dimensional regular grid of potential hypocenter locations was generated below the region where the seismic stations are located. In this study, we chose the middle-America trench axis as the reference direction. Thus the grid was rotated 15° clockwise from the north. The optimal $140 \times 60 \times 60\ km^3$ grid has 5 km increments in the three Cartesian directions and was located about 130 km away from the trench

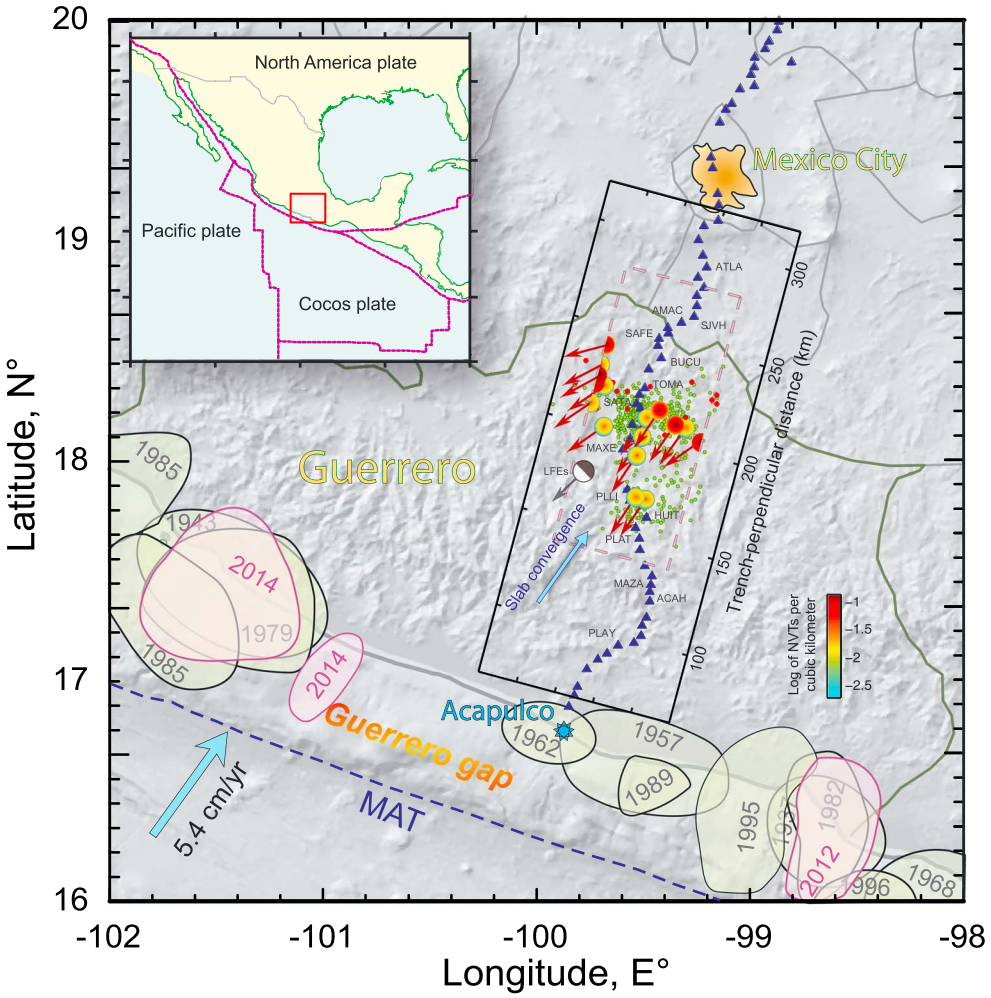

Figure 1. Study region and tectonic setting. Colored circles with red arrows represent NVT locations and mechanisms (i.e., slip directions) from this study. The figure also shows NVT epicenters (green dots) determined by *Husker et al.* [2012]; LFE epicenters (red dots) and the associated focal mechanism (gray beach ball) determined by *Frank et al.* [2013]; the MASE array stations (blue triangles) used in this study (i.e., those inside the black rectangle); the horizontal projection of the 3-D hypocentral lattice used by the TREP method (dashed rectangle); and the rupture area of major earthquakes in Mexico (shaded forms).

(dashed rectangle, Figure 1). For each grid node, a set of three-component double-couple high-frequency seismograms for horizontal point dislocations (i.e., the convolutions of the Green tensor spatial derivatives and the moment density tensor) with different rake angles were computed between the node and each site of the 42 available stations. Assuming a fault strike of 285° (i.e., the trench axis azimuth) and given the slip directions already observed in the region for LFE [*Frank et al.*, 2013], the rake angles ranged between 30° and 150° with a 10° increment. To compute the synthetic seismograms database, we used the wave number method [*Bouchon and Aki*, 1977] considering a layered elastic medium [*Campillo et al.*, 1996] and included the crustal intrinsic attenuation by means of frequency-dependent Q factors empirically determined by *García et al.* [2004], both suitable for the study region. More than 7.4 million point source synthetic seismograms were generated and saved in a database prior to the inversions for the whole grid and set of stations.

2.1. Energy and Particle Motion Polarization Estimates

The energy spatial distribution of a wavefield mainly depends on the source location and mechanism; however, site, scattering, and anelastic effects may also affect seismograms depending on the frequency band of interest. For these reasons, to compute the NVT energy distribution along the station array, we

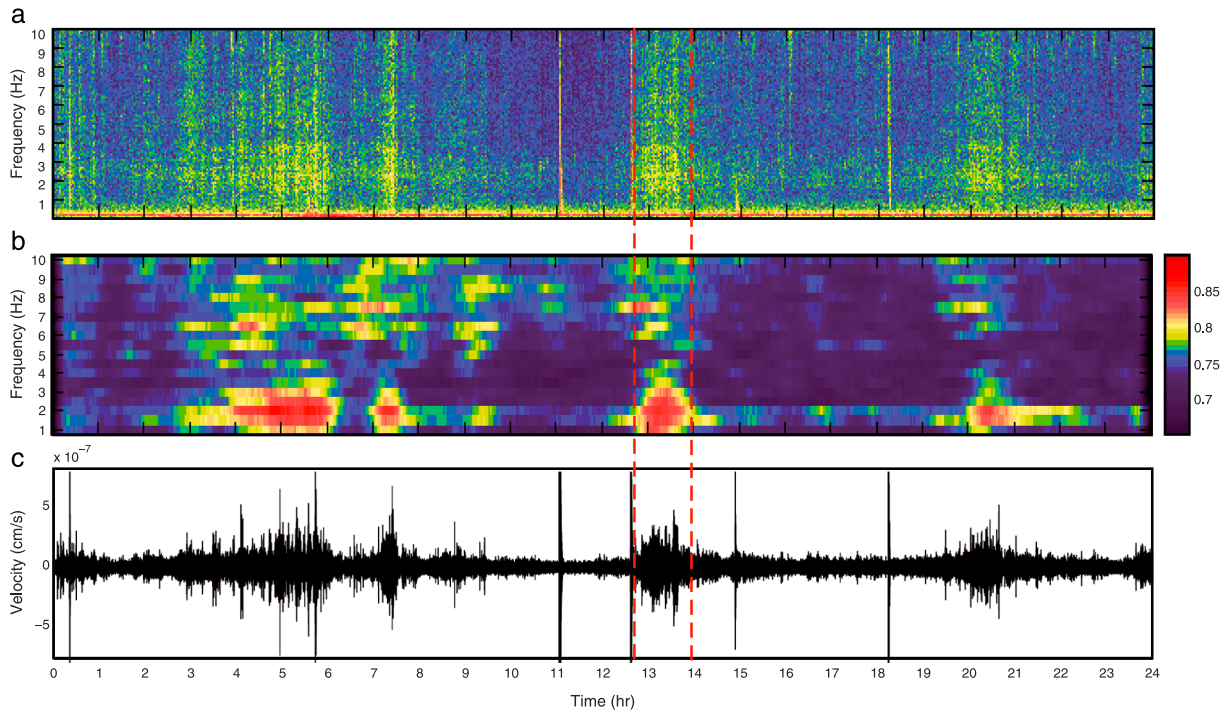

Figure 2. Spectral analysis of a 24 h seismogram recorded on 6 March 2005 in the north-south component of station SATA (Figure 1). (a) Energy spectrogram of the signal; (b) rectilinearity spectrogram of the particle motion (see section 2.1); and (c) 1–2 Hz band-pass-filtered signal. Vertical dashed lines depict the NVT located in Figure 3a.

followed the procedure introduced by *Kostoglodov et al*. [2010] and used by *Husker et al*. [2012] to locate NVT epicenters in the same region. The spectral signature of tremors in Guerrero emerges between 0.5 and 10 Hz (Figure 2a), although the signal-to-noise ratio is highest in the range of 1 to 2 Hz along most of the MASE stations [*Husker et al*., 2010]. After removing the trend and mean of the signals, we proceeded as follows: (1) filtered the three components of the observed seismograms in the 1–2 Hz bandwidth, (2) applied the corresponding site effect correction factors determined by *Husker et al*. [2010], (3) computed the square velocities per component, (4) applied a 10 min window median filter to smooth the resulting time series, and (5) computed the energy on each station, *e*, as the time cumulative values. For a given tremor episode, we thus generated three component energy values per station to finally obtain the three-dimensional energy distribution along the station array. Figures 3b and 3e, and Figures S1b and S1e in the supporting information, show some examples of energy distributions of tremors following this technique.

Similar to gravity anomalies [*Telford et al*., 1990], the shape of the energy functions (i.e. the width and slopes) is primarily controlled by the source distance. The wider and smoother the function, the farther is the source. Therefore, to improve the hypocentral depth resolution of the location technique, we incorporated the energy spatial derivatives approximated as the ratio of the energy difference between each pair of stations and the distance separating them (Figures 3c, 3f, S1c, and S1f).

Depending on the seismic array configuration, the energy distribution in the three components may not uniquely solve for the source location and mechanism. In our case, given the stations alignment (Figure 1, array geometry), this problem becomes critical. For this reason, we also analyzed the particle motion polarization ellipsoids, which have essential and complementary information about these source properties. We thus used the method proposed by *Flinn* [1965] and *Jurkevics* [1988] that has been proved to be a powerful tool for analyzing NVTs in Cascadia [*Wech and Creager*, 2007]. By solving the eigenproblem of the data covariance matrix, the method allows to determine the rectilinearity of the ground motion and the orientation of the corresponding polarization ellipsoid. The direction of the eigenvector associated with the largest eigenvalue (from now on referred as the main eigenvector) corresponds to the direction of the largest ellipsoid semiaxis, while the degree of rectilinearity, which ranges between 0 (spherical motion) and 1 (linear motion),

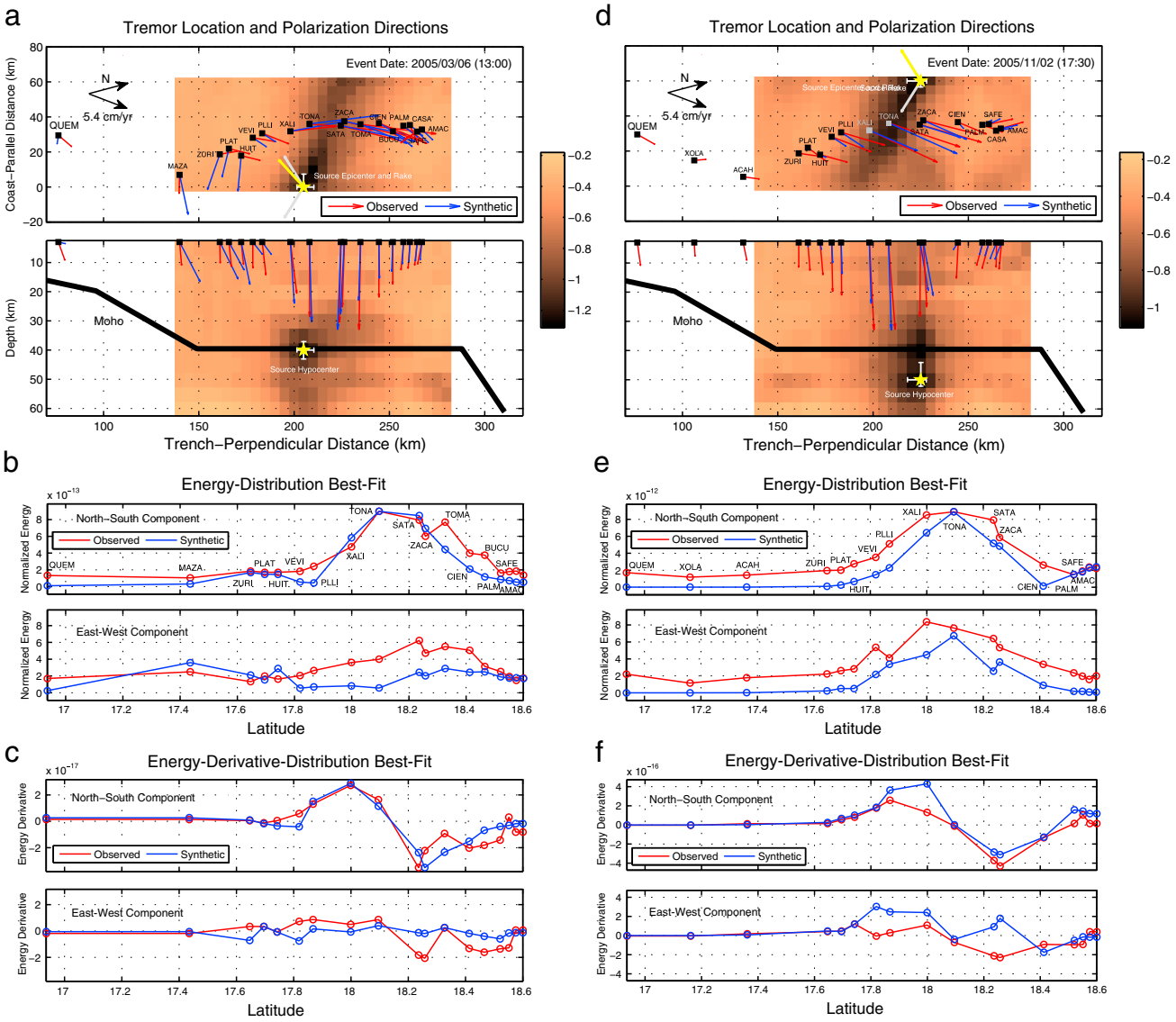

Figure 3. Location of two NVTs recorded on (left column) 6 March 2005 and (right column) 2 November 2005 using the TREP method. (a and d) Horizontal and vertical sections of cost function $\mathcal{Q}$ (background colors) across the best hypocenter location (yellow stars), location uncertainties (white bars), and rake angle searching range (gray arrows), observed and synthetic particle motion polarization directions (red and blue arrows; the arrow lengths are proportional to the NVT energy), and best solutions slip directions (yellow arrows); (b and e) best fits for the energy distribution along the station array; and (c and f) best fits for the spatial derivatives of the energy distributions.

is given by the combination $1 - [(\lambda_2 + \lambda_3)/2\lambda_1]$, where $\lambda_1 > \lambda_2 > \lambda_3$ and represent the three eigenvalues [*Jurkevics*, 1988]. Figure 2a shows the 24 h energy spectrogram of 6 March 2005 between 0.5 and 10 Hz at station SATA along with the corresponding rectilinearity spectrogram (Figure 2b) and the 1–2 Hz north-south filtered seismogram (Figure 2c). One main observation emerges: although the degree of motion rectilinearity is moderate, there is clear correlation in time and frequency between both spectrograms during tremor episodes (e.g., between 4 and 6 h, 7 and 7.6 h, 12.8 and 13.9 h, and 20 and 21 h). This implies that the ground motion polarization is dominated by coherent tremor signals (i.e., above the ambient seismic noise) and that such a seismic attribute could be used to detect NVT in future investigations. However, the direction of particle motion polarization may be affected by path and site effects. For this reason, we tested the methodology by determining the *P* wave polarization in the same frequency band (i.e., 1–2 Hz) of a normal-faulting regular earthquake registered on 26 May 2005, along the same station array. Results are shown in the supporting information (Figure S4), where we see that, in accordance with theoretical expectations, the polarization

direction in most of the stations points toward the hypocenter (i.e., it is ray parallel) as determined by *Pacheco and Singh* [2010]. We thus conclude that path and site effects are negligible for this observable (polarization direction) in the frequency range 1–2 Hz. To compute the rectilinearity of tremors, we used a 5 s moving window with time increments of 2 s and then applied a 10 s median filter over the resulting time series for each 0.5 Hz frequency band. Despite the almost continuous spectral signature of tremors, their polarization patterns are segmented in two frequency bands, one from 1 to 3 Hz and another from 5 to 9 Hz. This observation opens interesting questions about the nature of tremor sources that go beyond the scope of the present work, since we focused on polarization estimates in a frequency range of 1 to 2 Hz (i.e., the same as for the energy estimates) to locate the events.

We used the azimuthal direction of the largest polarization ellipsoid axis as the particle motion polarization metric in the location technique. This direction is given by the horizontal projection of the main eigenvector. Once projected, the horizontal polarization vector (HPV) is normalized to become proportional to the total energy on each site, as required by the cost function described in the next section. Figures 3 and S1 show the HPV along the array for four different NVTs and how the polarization azimuth changes from one event to the other.

2.2. Observable Metrics and Cost Function

As mentioned earlier, the location technique looks for the three hypocentral coordinates and the rake angle that minimize $\mathcal{Q}$, a compound cost function. This function depends on three different metrics, all of them computed in the same manner for the observed and synthetic data. The metrics are (1) the spatial energy distribution in the three components; (2) their corresponding spatial derivatives; and (3) the azimuth of the particle motion polarization direction. To compute the misfit between observed and synthetic data for metrics 1 and 2, we first normalize the energy and derivative distributions along the station array to their corresponding maximum absolute values in the three components. The misfit of the energy metric is then given by $\mathcal{E} = \sqrt{\sum_{i=1}^{n} (e_o - e_s)^2}$, i.e., the $\mathcal{L}2$-norm, where e_o and e_s are the observed and synthetic energy series in the three components, respectively, and n is the number of stations multiplied by three. Similarly, the misfit of the derivative metric is $\mathcal{D} = \sqrt{\sum_{i=1}^{n} (d_o - d_s)^2}$, where d_o and d_S are the observed and synthetic energy derivative series, respectively. The misfit of the polarization azimuth is defined as $\mathcal{P} = \sum_{i=1}^{n} (c_i \| \hat{p}_o - \hat{p}_s \|)$, i.e., the $\mathcal{L}1$-norm, where $\hat{p}_o$ and $\hat{p}_s$ are the horizontal projections (i.e., two-dimensional unit vectors) of the observed and synthetic main eigenvectors, respectively, and c_i are normalized weighting factors proportional to the total energy along the array (i.e., $0 < c_i < 1$ such that $c_i = 1$ at the station where the energy is maximum). These factors properly weight the polarization misfit depending on the amount of energy at every station. Finally, to establish a well-balanced cost function, $\mathcal{Q}$, combining all metric misfits, we define $\mathcal{Q} = \langle \hat{\mathcal{E}}, \hat{\mathcal{D}}, \hat{\mathcal{P}} \rangle$ as the average of the three misfit functions defined above after carrying out the following normalization. Let function $\mathcal{F}$ be $\mathcal{E}$, $\mathcal{D}$, or $\mathcal{P}$. Then, normalized function $\mathcal{F}$ is given by $\hat{\mathcal{F}} = [\mathcal{F} - \min(\mathcal{F})]/[\max(\mathcal{F}) - \min(\mathcal{F})]$. This definition has been found to optimize the problem resolution by maximizing the gradient of $\mathcal{Q}$ (i.e., the method resolution) in the surroundings of its absolute minimum. This can be clearly seen in Figure S5 of the supporting information, where we compare inversion results for each observable with those yielded by the joint inversion.

2.3. Location Technique Verification

In this section we introduce a novel tremor-like source model that is approximated by means of a finite difference approach. This model is then used to generate theoretical data for several synthetic inversion tests in order to assess and verify the TREP location method introduced in previous sections.

2.3.1. Nonvolcanic Tremor Source Model

We developed a 3-D quasi-dynamic source model to simulate tremor-like seismograms by means of a finite difference approach [*Cruz-Atienza*, 2006; *Cruz-Atienza et al*., 2007]. Although the model does not aim to describe the physics of NVT sources, it does provide a means to calculate sustained tremor-like signals (Figure 5a) along the MASE array within a heterogeneous Earth model (i.e., the structure by *Campillo et al*. [1996]) to be used as the "observed data" in our location technique.

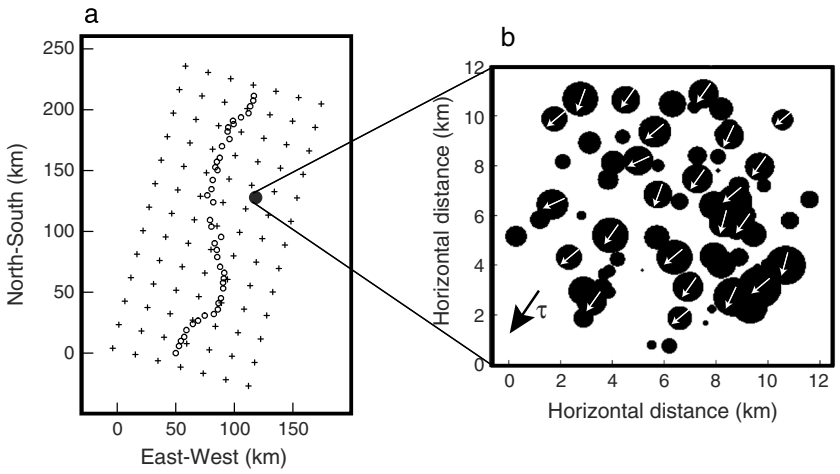

Figure 4. (a) MASE station array (circles, see Figure 1) and hypocentral lattice (down-sampled to a grid size of 20 km for visualization purposes; crosses) used in the synthetic inversion tests; and (b) penny-shaped cracks with variable shear prestress fields, $\boldsymbol{\tau}$ (white arrows) around a main direction (black arrow).

Since the Earth model we have considered is a simple 1-D layered medium, in order to introduce random variability in the simulated wavefield as observed in the real Earth due to scattering effects, the synthetic source is composed by 250 quasi-dynamic penny-shaped horizontal cracks following a spherical Gaussian distribution (with a radius of 5 km and a σ of 1 km) (Figure 4b) with a constant (radial) rupture speed (2.9 km/s, i.e., 0.8 times the *S* wave speed at 40 km depth) and a constant stress drop (0.5 bar). The stress breakdown process during the cracks rupture propagation is governed by a time-weakening friction law [*Andrews*, 2004] with a characteristic time of 0.6 s. The shear prestress (i.e., initial fault tangential traction) orientation varies randomly between cracks (i.e., ± 15°) (white arrows in Figure 4b) around a main prescribed direction (black arrow in Figure 4b) so that the slip direction (i.e., the rake angle) also varies in space from one crack to another. The radiuses of the cracks are also randomly generated with a Gaussian distribution around a value of 1 km and a σ of 0.5 km (black circles in Figure 4b). The rupture initiation time per crack is randomly set between the starting and ending simulation times (i.e., between 0 and 80 s). The source model is numerically approximated by means of a 3-D partly staggered finite difference scheme designed to simulate the dynamic rupture of faults [*Cruz-Atienza*, 2006; *Cruz-Atienza et al*., 2007]. The numerical model introduced by these authors has been adapted to the source features mentioned above and used with a grid size of 150 m and a time step of 0.015 s so that, considering the lowest *S* wave velocity in our crustal model (i.e., 3.1 km/s) [*Campillo et al*., 1996], the method guarantees a good numerical accuracy up to 2 Hz (i.e., 10 grid points per minimum wavelength) [*Bohlen and Saenger*, 2006].

2.3.2. Synthetic Inversion Results

Using this source model, we have generated tremor-like synthetic seismograms for frequencies below 2 Hz (e.g., see Figure 5a for the station XALI) along the MASE array (Figures 1 and 4a), which are the frequency bandwidth and the station array used to analyze real data in this present work. Results for two synthetic inversion tests are illustrated below, where the target sources have the same epicenters (green stars in Figures 6a and 6e) but different depths (i.e., 30 and 40 km) and prestress directions (i.e., main azimuths of 50° and 130°, green arrows in Figures 6a and 6e, respectively). The associated seismograms were inverted using a hypocentral grid with 5 km increments in the three Cartesian directions (crosses in Figure 4a).

Figure 6 shows the results for the best fit solution models yield by the two synthetic inversions. In the third and fourth rows (i.e., Figures 6c, 6d, 6g, and 6h), we find comparisons between the "observed tremors" (red) and the synthetic data (blue) for the energy distributions and the associated spatial derivatives. The overall fits in the three components are remarkably good. Relative amplitudes between NS and EW signals are self explained as well as the derivative profiles, which control the shape of the energy functions and thus the source depth. It is interesting to emphasize that, although both epicenters were collocated, the energy maxima is spatially shifted from one event to another. While the maximum of the NS component in the

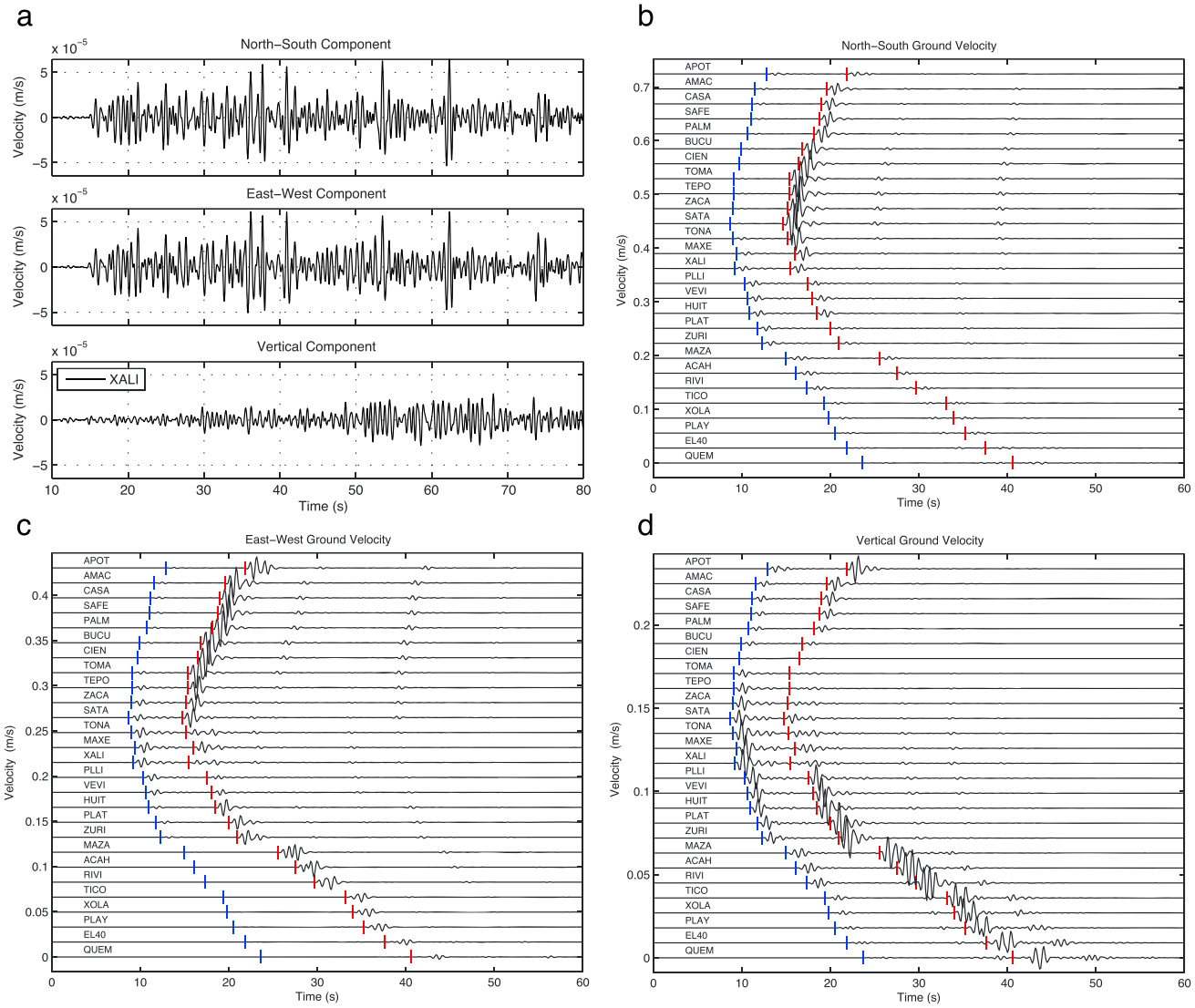

Figure 5. (a) Synthetic tremor-like seismograms computed at station XALI (see Figure 6) with the source model described here; and (b–d) synthetic seismograms in the three components along the station array (Figure 4) corresponding to the best Green functions and source mechanism found by the TREP method in the inversion test shown in the left column of Figure 6. The blue and red lines depict the *P* and *S* wave arrival times, respectively.

first event (i.e., with rake of 50°, Figure 6c) lies around 215 km from the trench, the maximum in the second event (i.e., with rake of 130°, Figure 6g) was about 20 km farther inland. This is even clearer in the EW components, where the maxima of both NVTs are shifted at about 50 km. This means that the energy spatial distribution is controlled by the hypocenter location and the source mechanism. On the other hand, notice how the particle motion polarization direction is very sensitive to the hypocentral depth and slip direction (compare horizontal vectors for both events, Figures 6a and 6e). Actually, different tests have demonstrated that including the polarization azimuth as an observable in the inversion technique is critical for uniquely solving the source mechanism and location (see Figure S5). Arrows in the vertical sections are only indicative of the particle motion ellipsoid inclination and were not used in the inversion. Cross sections of function $\mathcal{Q}$ passing through the best fit hypocenter locations (color maps) reveal that the minima of the functions coincide with the target source locations (i.e., those used to generate the observed data; compare yellow and green stars) and that the NVT mechanisms have been retrieved (compare yellow and green arrows). Other tests for different mechanisms and source locations along the array yielded similar results proving that, although resolution is significantly better in the horizontal directions (compare horizontal and vertical

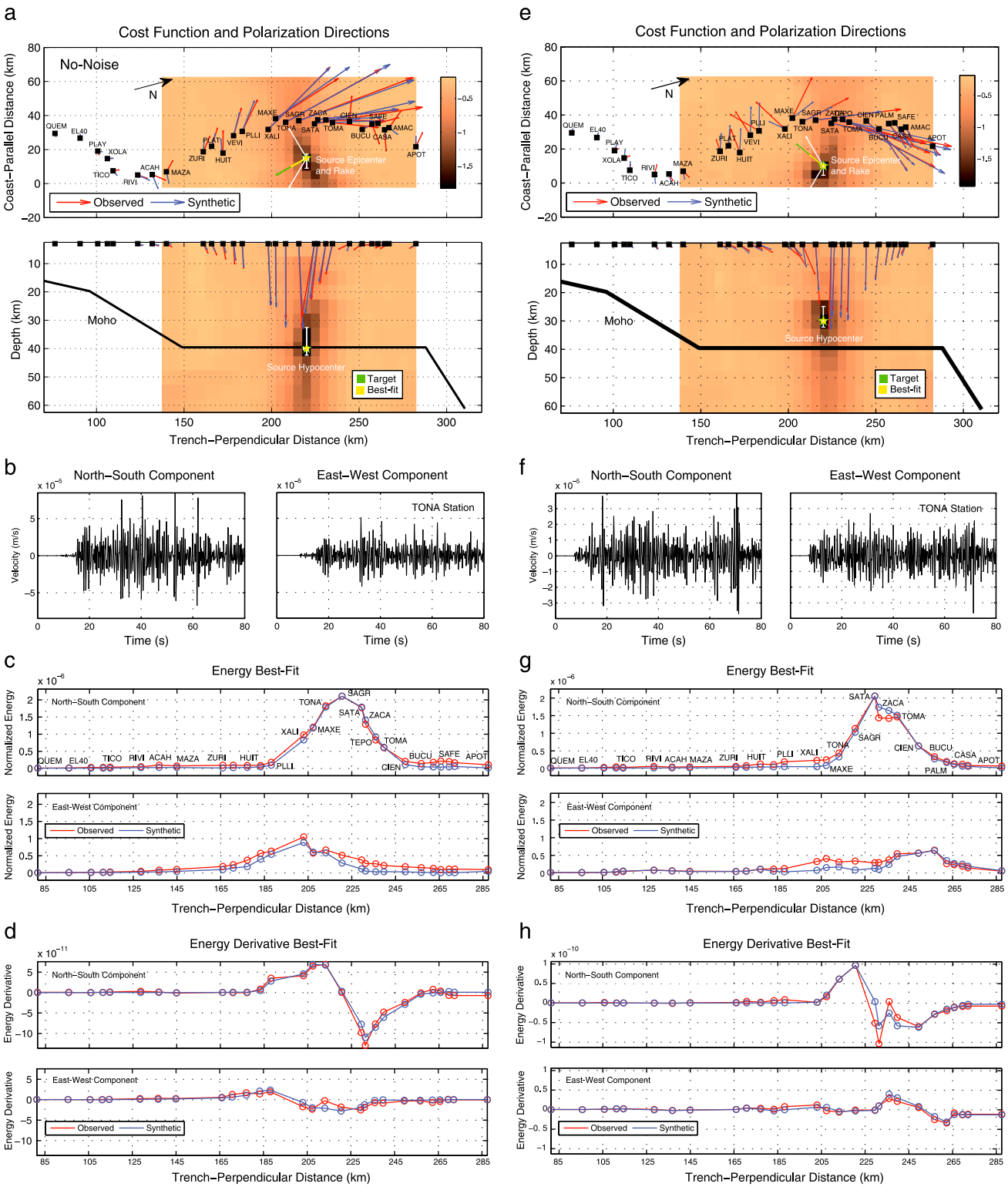

Figure 6. Location of two NVTs tremor-like synthetic sources (green stars and arrows) using the TREP method. (a and e) Horizontal and vertical cross sections of cost function $\mathcal{Q}$ (background colors) through the best hypocenter location (yellow stars), observed and synthetic particle motion polarization directions (red and blue arrows), and best solution slip directions (yellow arrows); (b and f) synthetic tremor seismograms in station TONA; (c and g) best fits for the energy distribution along the station array; and (d and h) best fits for the spatial derivatives of the energy distributions.

gradients of function $\mathcal{Q}$, see next section), the hypocentral depth and source mechanism are retrieved in all synthetic cases.

It is important to point out some implications of our synthetic inversion tests. All results were obtained assuming the same 1-D layered medium to compute the synthetic and the "observed" data. However, when comparing the misfit metrics for the best-fit point-source synthetic seismograms (Figures 5b–5d) with those for the synthetic tremor (Figure 5a), it is clear that our tremor-like source model has intrinsic properties that make the radiated wavefields from both kinds of sources remarkably different. This is due to several factors such as (1) the volumetric support of the tremor source, (2) the variable prestress conditions in the penny-shaped cracks, (3) the diffracted waves at the crack edges (i.e., stopping phases), and (4) the randomly generated rupture times of the cracks. In spite of these fundamental differences in the physics of both kinds of sources, our synthetic inversion tests have shown that the wavefield from simple point dislocation sources is able to explain satisfactorily the tremor-like signal properties we have selected by correctly retrieving both the target source locations and mechanisms.

2.3.3. Uncertainty in Source Location and Mechanism

Since we know neither the location of real NVTs nor their actual source mechanisms, a reasonable way to gain confidence in the TREP method is to quantify its formal error through synthetic inversion tests. Whether unmodeled effects or incomplete parameterization by TREP introduce large location errors is difficult to quantify. However, the synthetic NVT seismograms, which are "realistic" in the sense that they do not correspond to a single-point dislocation source (as TREP intrinsically assumes to fit the observed metrics), can be used to study the effect in the locations (and source mechanism) of both random seismic noise and some wavefield unmodeled features, such as the cumulative effect of quasi-dynamic cracks with radial rupture propagation.

To this purpose we have performed hundreds of synthetic inversions by adding random noise in the frequency band of interest (1–2 Hz) with different signal-to-noise ratios (SNR) to the "observed" data. The noise has the same amplitude in the three components of all stations so that the mean of its absolute value is equal to 1/SNR times the mean of the tremor signal in the component with maximum energy of the station array. Figures S2 and S3 of the supporting information show noisy seismograms for different SNR with the associated location results. The optimal way to quantify the location errors is by analyzing the distribution of hypocentral mislocations yielded by the inversions with respect to the target solution as a function of SNR. Then, if the distributions of mislocations were Gaussian, the associated standard deviations would provide a good estimate of error. However, except for SNR ≤ 2, which is an extreme value that prevents a majority of tremors to be detected in real seismograms, most tests for SNR > 2 yielded the right hypocentral locations (i.e., single-value unimodal distributions at zero mislocation). Similar results were obtained for the source mechanism, which revealed to be the most robust parameters of the inversion. Given the spatial increment of the hypocentral grid (5 km) this means that, provided that SNR > 2, the location error by TREP in the three components is smaller than ~2.5 km. Nevertheless, although TREP found the right locations in those cases, the shape (i.e., the gradient) of the cost function $\mathcal{Q}$ depends on the SNR, as can be seen in Figures S2 and S3.

Thus, following *Maeda and Obara* [2009], we took the method's resolution as a fair manner to estimate the uncertainty in the source parameters. The steeper $\mathcal{Q}$ in the surroundings of its global minimum, the higher is the resolution and the smaller should be the uncertainty in the estimated parameters. To quantify the shape of $\mathcal{Q}$ as a function of SNR we measured, along the three components, the distance to the global minimum of the points where $\mathcal{Q}$ becomes twice as large as its minimum (i.e., where the misfit error becomes 100% larger than its minimum value). Since $\mathcal{Q}$ is not necessarily symmetric with respect to the minimum, such resolution length (RL) may differ from one to the other side of the minimum. This can be seen, for instance, in Figures 3 and S1 (white bars passing across the hypocenters). In the following, we will consider as the resolution length per component, the average of both distances in the associated direction. In the top two panels of Figure 7 we gathered the results from the synthetic inversions considering a large range of SNR and number of random trials (i.e., 100 trials per SNR value equal to 2.0, 2.5, 3.0, 3.5, 4.0, 4.5, 5.0, and 10.0).

Figure 7a shows the resolution lengths in the three components (three different colors) as a function of the variance reduction (VR), as defined by *Maeda and Obara* [2009] (i.e., $\mathrm{VR} = 100 \cdot (1 - \mathcal{Q}_{min})$). Circles with black crosses indicate the inversions where SNR ≤ 2.0. As found by Maeda and Obara, the larger the VR, the smaller is the RL and thus the parameter's uncertainty. Notice that RL ≤ 8.0 km for SNR > 2.0 in the three

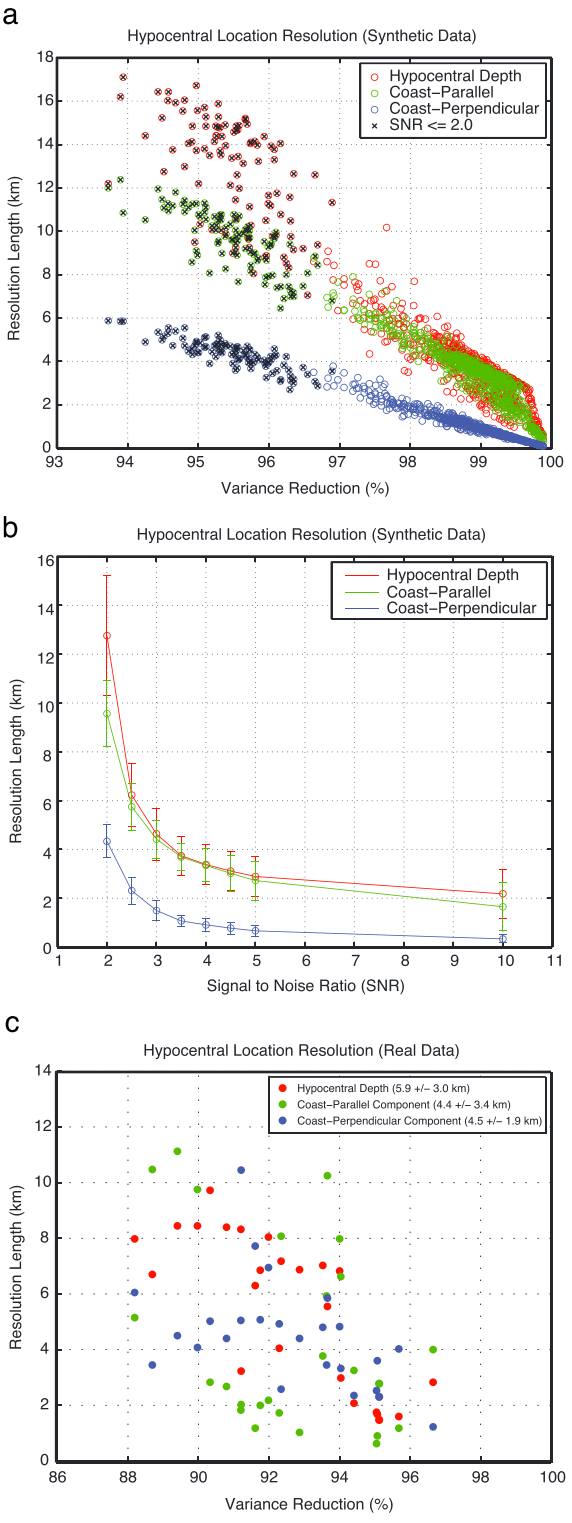

Figure 7. Analysis of location uncertainties. (a) Resolution lengths (RL) per component (different colors) as a function of variance reduction (VR) for 800 synthetic inversion tests with signal-to-noise ratios (SNR) ranging from 2 to 10. The crosses indicate those values for inversions with SNR $\leq$ 2.0. (b) Average RL values (circles) with $\pm 1\sigma$ (vertical bars) per SNR for the three components (different colors) of the same synthetic inversions. (c) Same estimates as in Figure 7a but for the entire population of real NVT analyzed in this work.

components. As expected, the resolution is highest along the axis of the station array (i.e., coast perpendicular coordinate, blue circles). In order to make useful this exercise for real data, Figure 7b presents the average resolution lengths (circles) along with the associated standard deviations (vertical bars) per value of SNR. Resolution is highly sensitive to low SNR values, so that RL becomes larger than ~6 km for noisy signals with SNR $\leq$ 2.5. Since these results where calculated using synthetic data from the tremor model introduced in section 2.3.1, they only tell us that seismic noise will significantly degrade the location resolution of real signals that meet such condition. In other words, meeting the condition SNR $\geq$ 2.5 is a necessary but not sufficient attribute that real tremors must have to guarantee a resolution length smaller than ~6 km.

3. Location of Nonvolcanic Tremors in Guerrero

We have applied the TREP technique to 26 tremor episodes in the state of Guerrero recorded between March 2005 and March 2007 along the Meso-America Seismic Experiment array [*MASE*, 2007] (triangles, Figure 1). These tremors were taken from the catalog developed by *Husker et al*. [2010]. Figures 3 and S1 show individual locations of four events and the associated misfits for the three inverted observables. The spectrograms and the signal from one of the NVT episodes (occurred on 6 March 2005, 12:40–14:00) are depicted with red dashed lines in Figure 2. Observed particle motion polarization azimuths (red arrows, Figures 3a and 3d) significantly change from one event to the other (e.g., compare station XALI, where the polarization azimuths differ about 35°, i.e., from ~85° to ~110°), indicating possible changes in the

source location and/or mechanism. Vertical polarization directions were not inverted due to low signal-to-noise ratios and are only indicative to better appreciate the energy distribution along the array (arrow lengths) (Figures 3a, 3d, S1a, and S1d, lower panels). The best solution models for both events satisfactorily explain the polarization azimuths (compare blue and red arrows), which have different locations but similar (although not identical) source mechanisms (i.e., rake angles). Similar results are obtained for locations shown in Figures S1a and S1d, where a simple shift of the epicentral location (without changing the source mechanism) is enough to explain the change of polarization and the energy-based metrics.

We recall that magnitudes of polarization vectors are proportional to the total energy, which is decomposed along the array in its three cardinal directions for inversion purposes (Figures 3b, 3e, S1b, and S1e). Vertical energy distributions are not shown because their amplitudes are about 2 times smaller than those of the horizontal components. Although fits between observed and synthetic metrics are not perfect, the energy spatial distributions are well explained by the best-fit solution sources (compare red and blue curves and symbols). Differences are primarily due to the ambient noise, which is only present in real seismograms. This can be clearly seen at stations located far from the epicenters, where the energy of the NVTs are negligible, as predicted by the theoretical blue curves (e.g., see stations QUEM and MAZA for the 6 March 2005 event, and stations QUEM to ZURI for the 2 November event). Despite the absence of noise in our model predictions, the overall shapes of the energy profiles are well explained, as confirmed by the quality of the energy derivative fits (Figures 3c, 3f, S1c, and S1f).

In order to determine the location uncertainty for each NVT of the whole population, we have quantified (1) the signal-to-noise ratio (SNR) and (2) the resolution lengths (RL) per component. Following our synthetic tests; to determine the SNR we took the ratio of the mean absolute amplitudes of noise and signal windows, and got SNR = 4.1 ± 1.6 for the population average. From Figure 7b we clearly see that such a noise level should not produce location errors larger than ~4 km. To make our results comparable to those reported by *Maeda and Obara* [2009], for computing the RL values we took the misfit threshold equal to $1.25 \cdot \mathcal{Q}_{min}$ (i.e., 25% above the minimum error). Estimates of RL per component for the events population are plotted in Figure 7c as a function of the variance reduction. As found by these authors (see their Figure 6b) and in agreement with our synthetic inversion results (Figure 7a), the larger the VR, the smaller is the RL. Average values per component are 5.9 ± 3.0 km, 4.4 ± 3.4 km, and 4.5 ± 1.9 km along depth, coast-parallel, and coast-perpendicular directions, respectively. Individual RL estimates are also indicated with white bars across the hypocenters in Figures 3a, 3d, S1a, and S1d. Although errors are larger in depth and may vary between events within the reported ranges, we conclude that location uncertainties in the three components are roughly the same and around 5 km.

Unlike the work by *Husker et al.* [2012], Figures 3a (bottom) and 3d (bottom) show that the tremor epicenters are not collocated with the maxima of the energy functions. For these two events, there is a spatial shift of about 20 km between them (either to the north or south direction). This is in accordance with our synthetic inversion tests (see Figure 6) and was expected because the approach used by *Husker et al.* [2012] did not consider the source radiation patterns. Tests we performed revealed that uniqueness of the inverse problem is strongly enhanced by the combination of the three observables (see Figure S5d). For instance, if the polarization azimuth is not inverted (Figures S5a and S5b), the energy-based observables may not solve the epicenter location along the array-perpendicular direction (i.e., the method yields two antisymmetric solutions with respect to the array; Figure S5a). Although in general our compound cost function exhibits prominent and unique minima in the horizontal plane, this is not always the case in depth. Figure 3d (bottom) shows an example where $\mathcal{Q}$ has two comparable minima, the absolute one at 50 km depth and a second one 10 km shallower (i.e., at the plate interface). Since we do not have arguments based on our location technique to determine which of the minima is more likely to be correct, interpretations must be done carefully.

Source model solutions for the whole set of NVT events are shown in Figures 1 and 8. Circles with 5 km radius (i.e., the location uncertainty determined above) represent tremor locations, and their colors correspond to the logarithm of the NVTs per cubic kilometer. The most recent locations of NVTs in the region by *Husker et al.* [2012] and low-frequency earthquakes (LFEs) by *Frank et al.* [2013] are also plotted in Figure 1 with green and red dots, respectively. Three main observations come out: (1) in accordance with the work by *Payero et al.* [2008] and *Husker et al.* [2012], our tremor locations are separated in two main groups, one at the "sweet spot" [*Husker et al.*, 2012], between 200 and 230 km from the trench, and another one closer to the trench at about

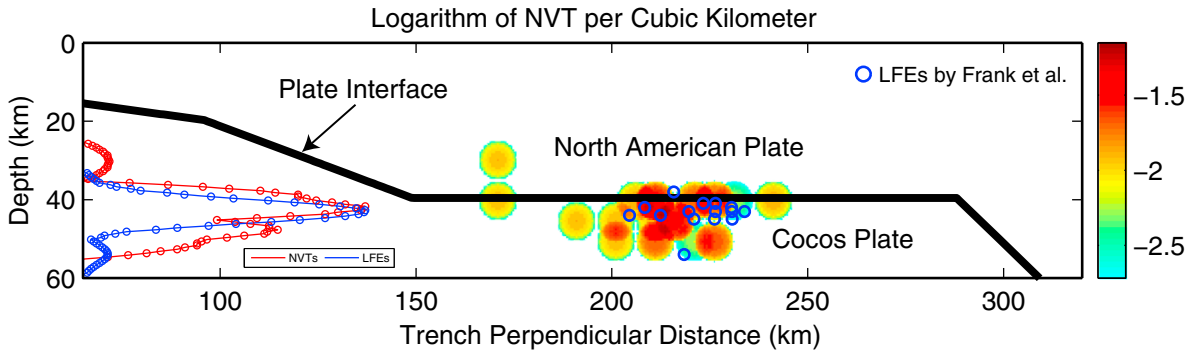

Figure 8. Locations of NVTs using the TREP method (colored circles) and LFEs by *Frank et al.* [2013] (blue circles) projected into a vertical trench-perpendicular cross section. On the left is the comparison of normalized histograms for both kinds of events (red and blue curves for NVTs and LFEs, respectively).

170 km; (2) fault mechanisms of both NVTs and LFEs are consistent between each other and subparallel to the Cocos plate convergence direction (compare red arrows with both gray and blue arrows); and (3) most of the LFEs reported by *Frank et al.* [2013] seem to be located farther from the trench than the NVTs.

Figure 8 shows our NVT locations (colored circles) compared with those for LFEs (blue circles) reported by *Frank et al.* [2013] projected into a vertical trench-perpendicular cross section. The interface between the Cocos and the North American plates is sketched with a black line following the geometry proposed by *Pérez-Campos et al.* [2008]. To make the comparison of foci locations clearer, in the left we show normalized histograms for both kinds of events as a function of depth (red and blue curves). Although the NVTs histogram is bimodal with a secondary peak at 48 km depth (i.e., inside the slab), both NVTs and LFEs have their maxima of occurrence around 43 km, indicating that most of the sources of these two kinds of signals originate at the same depths and probably on the plate interface. Because of the orientation of the cross section and since the alignment of NVTs at the sweet spot is not parallel to the trench (see Figure 1), the horizontal position of NVTs relative to LFEs may not be well appreciated in the figure. However, at least for the events reported here, it seems that most LFEs occur in the northern edge of the region where the NVT activity happens.

4. Discussion and Conclusions

In this study we have introduced the TREP method, which is a novel technique to locate and determine the source mechanism of NVT signals. Using energy-based and particle motion polarization metrics, the method simultaneously determines the location and mechanism of the tremor source that minimize a compound cost function considering frequency-dependent quality factors (Q) in a layered medium. The combination of different properties of the seismic wavefield allows TREP to satisfactorily solve both epicentral locations and hypocentral depths. Synthetic tests lead us to conclude that location errors by TREP due to seismic noise are smaller than 6 km provided that SNR $\geq$ 2.5 in the station with highest NVT energy. Besides, actual errors (i.e., resolution lengths) per component for the whole real-event population are 5.9 $\pm$ 3.0 km, 4.4 $\pm$ 3.4 km, and 4.5 $\pm$ 1.9 km along depth, coast-parallel, and coast-perpendicular directions, respectively. Based on previous research, we have assumed that tremors are produced by horizontal shear failures, which is a hypothesis that may also introduce location errors. However, this constrain may be easily relaxed in regions where no information of the source mechanism is available. Since the TREP technique does not require any temporal information of the observed wavefield (e.g., waveform templates), it can be also used to locate LFEs and VLFs provided that relative amplitudes between stations are preserved. This would provide the possibility of comparing focal locations and mechanisms of different signals (i.e., NVT, LFE, and VLF) by means of the same technique and thus have more confidence in their relative positions and origins.

Tremor amplitudes recorded in a station array depend upon several factors, such as the hypocentral distance and the attenuation, site, and scattering effects. However, if some stations lie in a nodal source direction, amplitudes may be negligible despite their proximity to the epicenter. As shown in this work, this is why considering the source mechanism is critical to properly locate tremors. One possible explanation of the NVT widespread locations reported by *Kao et al.* [2005, 2009] is that the SSA used by these authors detects and

locates events from stacked waveforms considering only theoretical travel times (i.e., relative move outs), which implies neglecting possible radiation patterns from double couples. Neglecting this possibility may lead to significant location errors (i.e., ~20 km mislocations in our case, see section 2.3.2), because the energy maxima do not necessarily coincide with the epicenters.

Using the TREP method, we determined the epicenters of 26 NVTs in Guerrero, which are consistent with previous studies in the region [*Payero et al*., 2008; *Husker et al*., 2012]. The epicenters are separated in two main groups, one at the "sweet spot" [*Husker et al*., 2012], between 200 and 230 km from the trench, and another one closer to the trench at about 170 km. However, hypocentral depths are clearly different as compared to the only available ones [*Payero et al*., 2008]. Our estimates show that sustained tremors are produced by shear failures near the plate interface (i.e., about 60% of the whole NVT sample) with rake angles that are subparallel to the Cocos-North America plates convergence direction. Thus, NVT locations in Guerrero are in agreement with independent depth and source mechanism estimates for LFEs by *Frank et al*. [2013], with a similar hypocentral depth distribution for both types of events with maxima at 43 km depth. This result further supports the idea proposed by *Shelly et al*. [2007] and *Ide et al*. [2007] stating that the NVTs have the same origin as the LFEs and that the NVTs are consistent with the SSEs source mechanism.

Our results also show a deeper region within the subducting slab at ~48 km depth (i.e., in the oceanic crust) with ~40% of the NVT activity. This suggests that intraslab NVT sources may exist in Guerrero and be related to the concentration of free fluids in the Sweet Spot as a consequence of the SSEs-induced strain fields inside the Cocos plate [*Cruz-Atienza et al*., 2011]. Although the NVT events considered here do not correspond to a complete catalog, our results suggest that there is almost no tremor activity in the continental crust. To assess whether transient reductions (i.e., nonlinear response) of the middle and deep continental rocks stiffness induced by the SSEs in Guerrero [*Rivet et al*., 2011, 2013] may trigger NVTs above the plate interface, a temporal and detailed analysis of the complete tremor catalogs of Guerrero should be undertaken.

Acknowledgments

We thank Christophe Morisset and Eiichi Fukuyama for fruitful discussions and suggestions, and Elena García Seco for scientific writing corrections. We also thank the Meso-America Subduction Experiment [*MASE*, 2007] for the data used in this study (http://www.gps.caltech.edu/~clay/MASEdir/data_avail.html). This work was possible thanks to the UNAM-PAPIIT grants IN113814 and IN110514, and the Mexican "Consejo Nacional de Ciencia y Tecnología" (CONACyT) under grants 130201 and 178058.

References

Andrews, D. J. (2004), Rupture models with dynamically determined breakdown displacement, *Bull. Seismol. Soc. Am.*, *94*(3), 769–775.

Beroza, G., and S. Ide (2011), Slow earthquakes and nonvolcanic tremor, *Annu. Rev. Earth Planet. Sci.*, *39*, 271–96.

Bohlen, T., and E. H. Saenger (2006), Accuracy of heterogeneous staggered-grid finite-difference modeling of Rayleigh waves, *Geophysics*, *71*, T109–T115.

Bostock, M. G., A. A. Royer, E. H. Hearn, and S. M. Peacock (2012), Low frequency earthquakes below southern Vancouver Island, *Geochem. Geophys. Geosyst.*, *13*, Q11007, doi:10.1029/2012GC004391.

Bouchon, M., and K. Aki (1977), Discrete wave number representation of seismic source wave fields, *Bull. Seismol. Soc. Am.*, *67*, 259–277.

Brown, J. R., G. C. Beroza, S. Ide, K. Ohta, D. R. Shelly, S. Y. Schwartz, W. Rabbel, M. Thorwart, and H. Kao (2009), Deep low-frequency earthquakes in tremor localize to the plate interface in multiple subduction zones, *Geophys. Res. Lett.*, *36*, L19306, doi:10.1029/2009GL040027.

Campillo, M., S. K. Singh, N. Shapiro, J. Pacheco, and R. B. Herrmann (1996), Crustal structure south of the Mexican volcanic belt, based on group velocity dispersion, *Geofis. Int.*, *35*, 361–370.

Cavalié, O., E. Pathier, M. Radiguet, M. Vergnolle, N. Cotte, A. Walpersdorf, V. Kostoglodov, and F. Cotton (2013), Slow slip event in the Mexican subduction zone: Evidence of shallower slip in the Guerrero seismic gap for the 2006 event revealed by the joint inversion of InSAR and GPS data, *Earth Planet. Sci. Lett.*, *367*, 52–60.

Cruz-Atienza, V. M. (2006), Rupture dynamique des failles non-planaires en différences finies, PhD thesis, p. 382, Univ. of Nice Sophia-Antipolis, France.

Cruz-Atienza, V. M., J. Virieux, and H. Aochi (2007), 3D finite-difference dynamic-rupture modelling along non-planar faults, *Geophysics*, *72*, doi:10.1190/1.2766756.

Cruz-Atienza, V. M., D. Rivet, V. Kostoglodov, A. L. Husker, D. Legrand, and M. Campillo (2011), Toward a unified theory of silent seismicity in Central Mexico, *Eos Trans. AGU, 92*, Fall Meet. Suppl., Abstract S23B–2264.

Dragert, H., K. Wang, and T. S. James (2001), A silent slip event on the deeper Cascadia subduction interface, *Science*, *292*, 1525–1528, doi:10.1126/science.1060152.

Flinn, E. (1965), Signal analysis using rectilinearity and direction of particle motion, *Proc. IEEE*, *53*, 1874–1876.

Franco, S. I., V. Kostoglodov, K. M. Larson, V. C. Manea, M. Manea, and J. A. Santiago (2005), Propagation of the 2001–2002 silent earthquake and interplate coupling in the Oaxaca subduction zone, Mexico, *Earth Planets Space*, *57*, 973–985.

Frank, W. B., N. M. Shapiro, V. Kostoglodov, A. L. Husker, M. Campillo, J. S. Payero, and G. A. Prieto (2013), Low-frequency earthquakes in the Mexican Sweet Spot, *Geophys. Res. Lett.*, *40*, 2661–2666, doi:10.1002/grl.50561.

García, D., S. K. Singh, M. Herraíz, J. F. Pacheco, and M. Ordaz (2004), Inslab earthquakes of central Mexico: *Q*, source spectra and stress drop, *Bull. Seismol. Soc. Am.*, *94*, 789–802.

Ghosh, A., J. E. Vidale, J. R. Sweet, K. C. Creager, and A. G. Wech (2009), Tremor patches in Cascadia revealed by seismic array analysis, *Geophys. Res. Lett.*, *36*, L17316, doi:10.1029/2009GL039080.

Husker, A., S. Peyrat, N. Shapiro, and V. Kostoglodov (2010), Automatic non-volcanic tremor detection in the Mexican subduction zone, *Geofis. Int.*, *49*(1), 17–25.

Husker, A. L., V. Kostoglodov, V. M. Cruz-Atienza, D. Legrand, N. M. Shapiro, J. S. Payero, M. Campillo, and E. Huesca-Pérez (2012), Temporal variations of non-volcanic tremor (NVT) locations in the Mexican subduction zone: Finding the NVT sweet spot, *Geochem. Geophys. Geosyst.*, *13*, Q03011, doi:10.1029/2011GC003916.

Ide, S., D. R. Shelly, and G. C. Beroza (2007), Mechanism of deep low frequency earthquakes: Further evidence that deep non-volcanic tremor is generated by shear slip on the plate interface, *Geophys. Res. Lett.*, *34*, L03308, doi:10.1029/2006GL028890.

Iglesias, A., S. K. Singh, A. R. Lowry, M. Santoyo, V. Kostoglodov, K. M. Larson, and S. I. Franco-Sánchez (2004), The silent earthquake of 2002 in the Guerrero seismic gap, Mexico (*Mw* = 7.6): Inversion of slip on the plate interface and some implications, *Geofís. Int.*, *43*(3), 309–317.

Ito, Y., K. Obara, K. Shiomi, S. Sekine, and H. Hirose (2007), Slow earthquakes coincident with episodic tremors and slow slip events, *Science*, *315*, 503–506, doi:10.1126/science.1134454.

Jurkevics, A. (1988), Polarization analysis of three-component array data, *Bull. Seismol. Soc. Am.*, *78*(5), 1725–1743.

Kao, H., and S.-J. Shan (2004), The source-scanning algorithm: Mapping the distribution of seismic sources in time and space, *Geophys. J. Int.*, *157*, 589–594.

Kao, H., S.-J. Shan, H. Dragert, G. Rogers, J. F. Cassidy, and K. Ramachandran (2005), A wide depth distribution of seismic tremors along the northern Cascadia margin, *Nature*, *436*, 841–844, doi:10.1038/nature03903.

Kao, H., S.-J. Shan, H. Dragert, and G. Rogers (2009), Northern Cascadia episodic tremor and slip: A decade of tremor observations from 1997 to 2007, *J. Geophys. Res.*, *114*, B00A12, doi:10.1029/2008JB006046.

Kostoglodov, V., A. Husker, N. M. Shapiro, J. S. Payero, M. Campillo, N. Cotte, and R. Clayton (2010), The 2006 slow slip event and nonvolcanic tremor in the Mexican subduction zone, *Geophys. Res. Lett.*, *37*, L24301, doi:10.1029/2010GL045424.

Legrand, D., S. Kaneshima, and H. Kawakatsu (2000), Moment tensor analysis of near-field broadband waveforms observed at Aso Volcano, Japan, *J. Volcanol. Geotherm. Res.*, *101*, 155–169, doi:10.1016/S0377-0273(00)00167-0.

Lowry, A. R., K. M. Larson, V. Kostoglodov, and R. Bilham (2001), Transient fault slip in Guerrero, southern Mexico, *Geophys. Res. Lett.*, *28*, 3753–3756.

Maeda, T., and K. Obara (2009), Spatiotemporal distribution of seismic energy radiation from low-frequency tremor in western Shikoku, Japan, *J. Geophys. Res.*, *114*, B00A09, doi:10.1029/2008JB006043.

MASE (2007), Meso America subduction experiment, *Caltech. Dataset.*, doi:10.7909/C3RN35SP.

Obara, K. (2002), Nonvolcanic deep tremor associated with subduction in southwest Japan, *Science*, *296*, 1679–1681.

Obara, K. (2010), Phenomenology of deep slow earthquake family in southwest Japan: Spatiotemporal characteristics and segmentation, *J. Geophys. Res.*, *115*, B00A25, doi:10.1029/2008JB006048.

Obara, K., H. Hirose, F. Yamamizu, and K. Kasahara (2004), Episodic slow slip events accompanied by non-volcanic tremors in southwest Japan subduction zone, *Geophys. Res. Lett.*, *31*, L23602, doi:10.1029/2004GL020848.

Obara, K., S. Tanaka, T. Maeda, and T. Matsuzawa (2010), Depth-dependent activity of non-volcanic tremor in southwest Japan, *Geophys. Res. Lett.*, *37*, L13306, doi:10.1029/2010GL043679.

Pacheco, J. F., and S. K. Singh (2010), Seismicity and state of stress in Guerrero segment of the Mexican subduction zone, *J. Geophys. Res.*, *115*, B01303, doi:10.1029/2009JB006453.

Payero, J. S., V. Kostoglodov, N. Shapiro, T. Mikumo, A. Iglesias, X. Pérez-Campos, and R. W. Clayton (2008), Nonvolcanic tremor observed in the Mexican subduction zone, *Geophys. Res. Lett.*, *35*, L07305, doi:10.1029/2007GL032877.

Pérez-Campos, X., Y. Kim, A. Husker, P. M. Davis, R. W. Clayton, A. Iglesias, J. F. Pacheco, S. K. Singh, V. C. Manea, and M. Gurnis (2008), Horizontal subduction and truncation of the Cocos Plate beneath central Mexico, *Geophys. Res. Lett.*, *35*, L18303, doi:10.1029/2008GL035127.

Radiguet, M., F. Cotton, M. Vergnolle, M. Campillo, A. Walpersdorf, N. Cotte, and V. Kostoglodov (2012), Slow slip events and strain accumulation in the Guerrero gap, Mexico, *J. Geophys. Res.*, *117*, B04305, doi:10.1029/2011JB008801.

Rivet, D., M. Campillo, N. M. Shapiro, V. Cruz-Atienza, M. Radiguet, N. Cotte, and V. Kostoglodov (2011), Seismic evidence of nonlinear crustal deformation during a large slow slip event inMexico, *Geophys. Res. Lett.*, *38*, L08308, doi:10.1029/2011GL047151.

Rivet, D., et al. (2013), Seismic velocity changes, strain rate and non-volcanic tremors during the 2009–2010 slow slip event in Guerrero, Mexico, *Geophys. J. Int.*, doi:10.1093/gji/ggt374.

Rogers, G., and H. Dragert (2003), Episodic tremor and slip on the Cascadia subduction zone: The chatter of silent slip, *Science*, *300*, 1942–1943, doi:10.1126/science.1084783.

Shelly, D. R., G. C. Beroza, S. Ide, and S. Nakamura (2006), Low-frequency earthquakes in Shikoku, Japan, and their relationship to episodic tremor and slip, *Nature*, *442*, 188–191, doi:10.1038/nature04931.

Shelly, D. R., G. C. Beroza, and S. Ide (2007), Non-volcanic tremor and low-frequency earthquake swarms, *Nature*, *446*, 305–307, doi:10.1038/nature05666.

Telford, W. M., L. P. Geldart, and R. E. Sheriff (1990), *Applied Geophysics*, Cambridge Univ. Press, Cambridge, U. K.

Vergnolle, M., A. Walpersdorf, V. Kostoglodov, P. Tregoning, J. A. Santiago, N. Cotte, and S. I. Franco (2010), Slow slip events in Mexico revised from the processing of 11 year GPS observations, *J. Geophys. Res.*, *115*, B08403, doi:10.1029/2009JB006852.

Wech, A. G., and K. C. Creager (2007), Cascadia tremor polarization evidence for plate interface slip, *Geophys. Res. Lett.*, *34*, L22306, doi:10.1029/2007GL031167.

Wech, A. G., and K. C. Creager (2008), Automated detection and location of Cascadia tremor, *Geophys. Res. Lett.*, *35*, L20302, doi:10.1029/2008GL035458.

Auxiliary material for

Non-Volcanic Tremor Locations and Mechanisms in Guerrero, Mexico, from Energy-based and Particle-Motion Polarization Analysis

Víctor M. Cruz-Atienza*, Allen Husker, Denis Legrand,
Emmanuel Caballero and Vladimir Kostoglodov

(*Corresponding author email: cruz@geofisica.unam.mx)

Instituto de Geofísica, Universidad Nacional Autónoma de México

Journal of Geophysical Research – Solid Earth
October 2014

In this Electronic Supplement we present complementary information regarding (1) location of real tremors (Figure A1), (2) resolution of the TREP method through synthetic inversion tests as a function of the signal to noise ratio (Figures A2 and A3), (3) path and site effects in the polarization azimuth (Figure A4), and (4) the benefits of combining the three observables in the inversion technique (Figure A5). Details of procedures and discussions are provided in the associated figure captions and the main text.

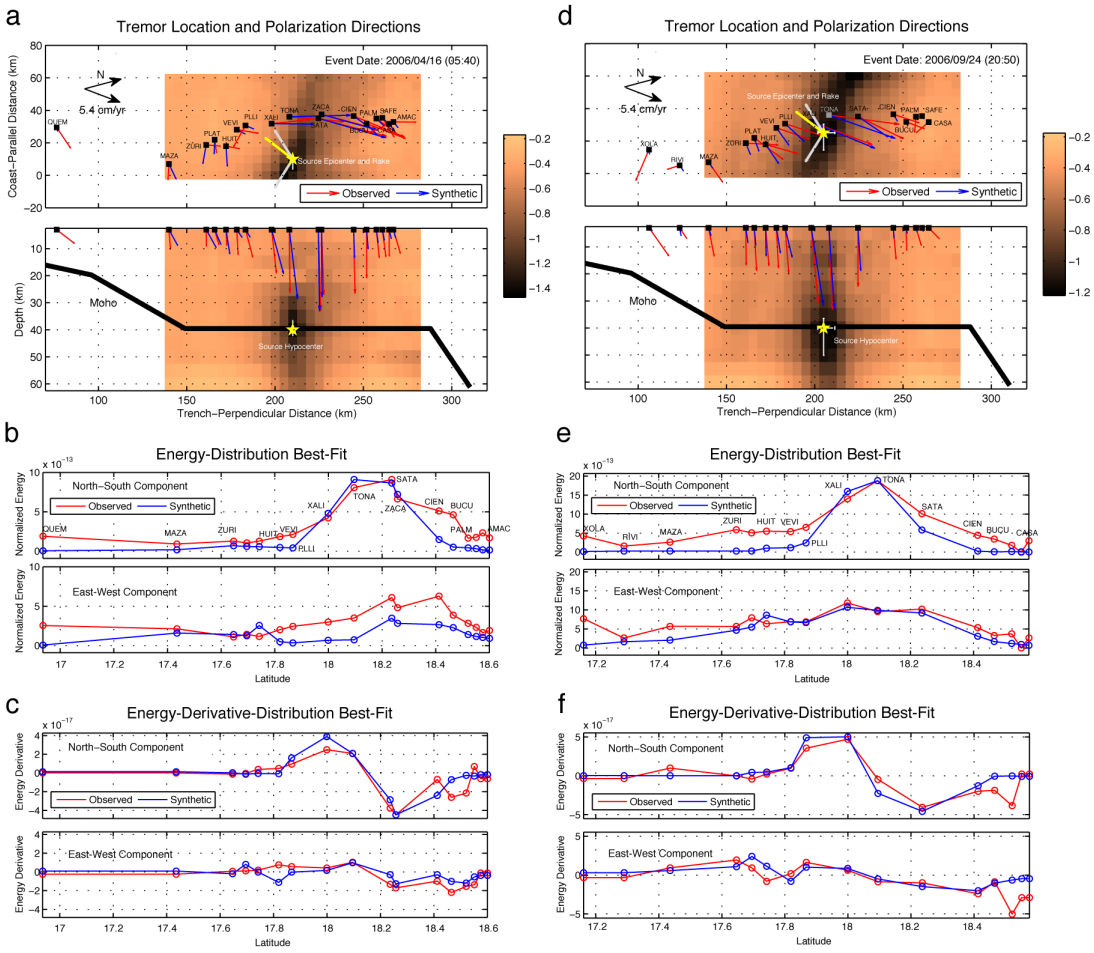

Figure A1 Location of two NVTs recorded on April 16, 2006 (left column) and September 24, 2006 (right column) using the TREP method. (a and d) Horizontal and vertical sections of cost function Q (background colors) across the best hypocenter location (yellow stars), location uncertainties (white bars) and rake angle searching range (gray arrows), observed and synthetic particle motion polarization directions (red and blue arrows), and best solutions slip directions (yellow arrows); (b and e) best-fits for the energy distribution along the station array; and (c and f) best-fits for the spatial derivatives of the energy distributions.

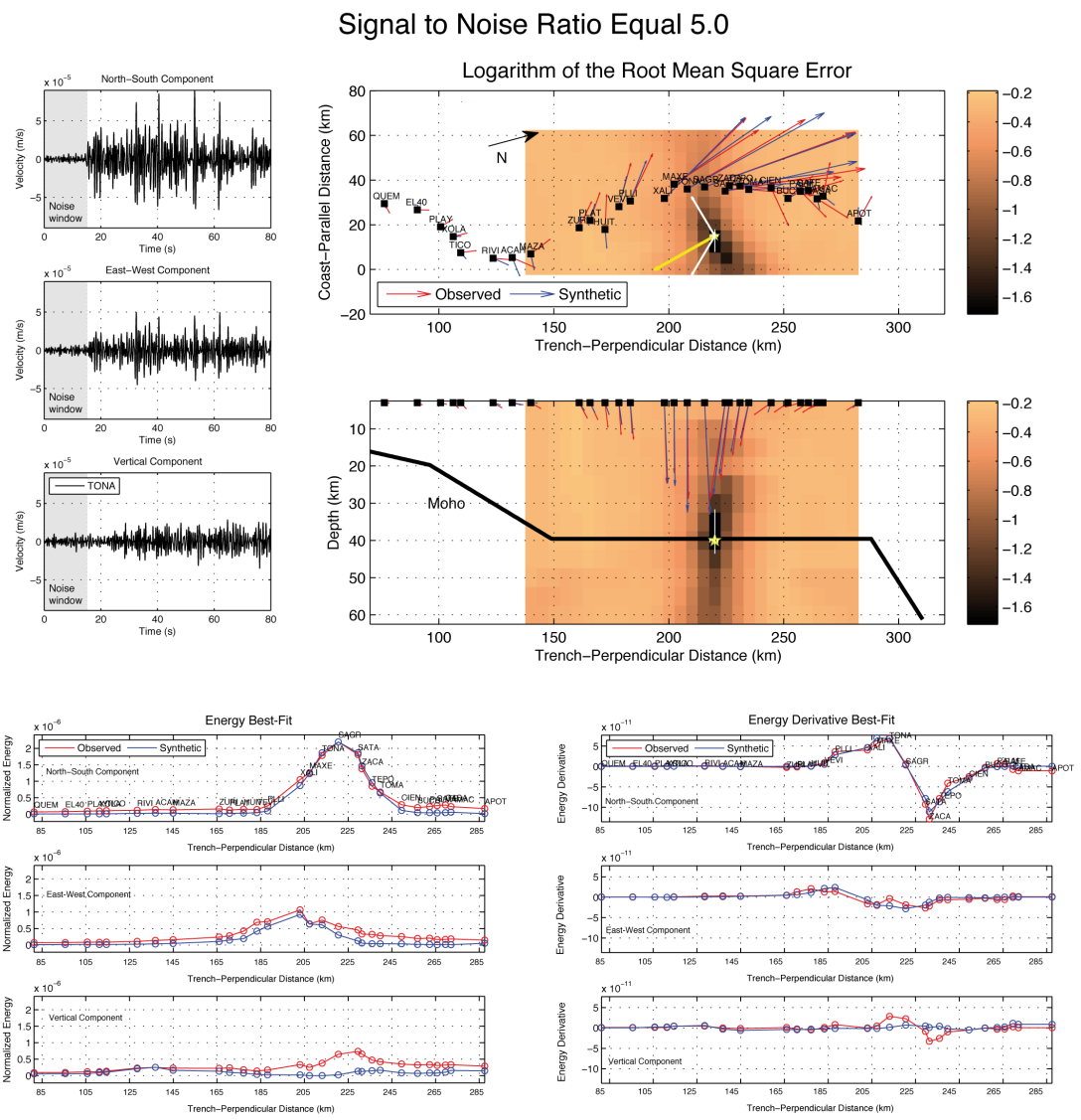

Figure A2 Location of two NVT tremor-like synthetic sources (green stars and arrows) using the TREP method. (Top left) Random seismic noise (gray bands) with a SNR = 5.0 has been added to the inverted signals. The signal to noise ratio (SNR) refers to the value at the station component where the NVT signal has its maximum amplitude (i.e., the north-south component above), which means that the SNR in the rest of the stations is smaller. (Top right) Horizontal and vertical cross-sections of cost function Q (background colors) through the best hypocenter location (yellow stars) and rake angle searching range (white arrows), observed and synthetic particle motion polarization directions (red and blue arrows), and best solutions slip directions (yellow arrows). (Bottom left) best-fits for the energy distribution along the stations array. And (bottom right) best-fits for the spatial derivatives of the energy distributions. Compare with Figure 6 (left column) of the main text.

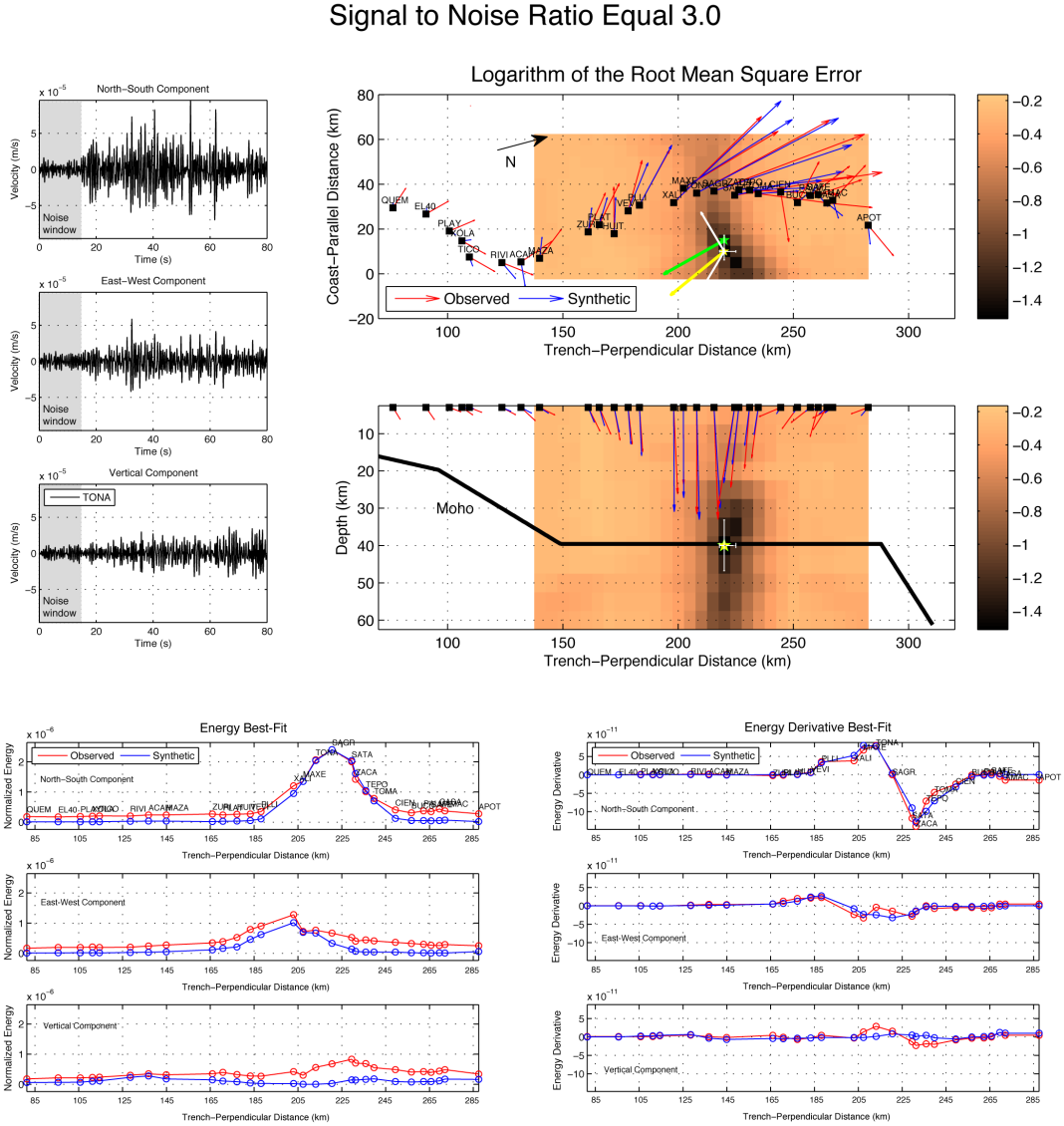

Figure A2 (continue) Same as the previous figure but for SNR = 3.0. Compare with Figure 6 (left column) of the main text.

Signal to Noise Ratio Equal 2.5

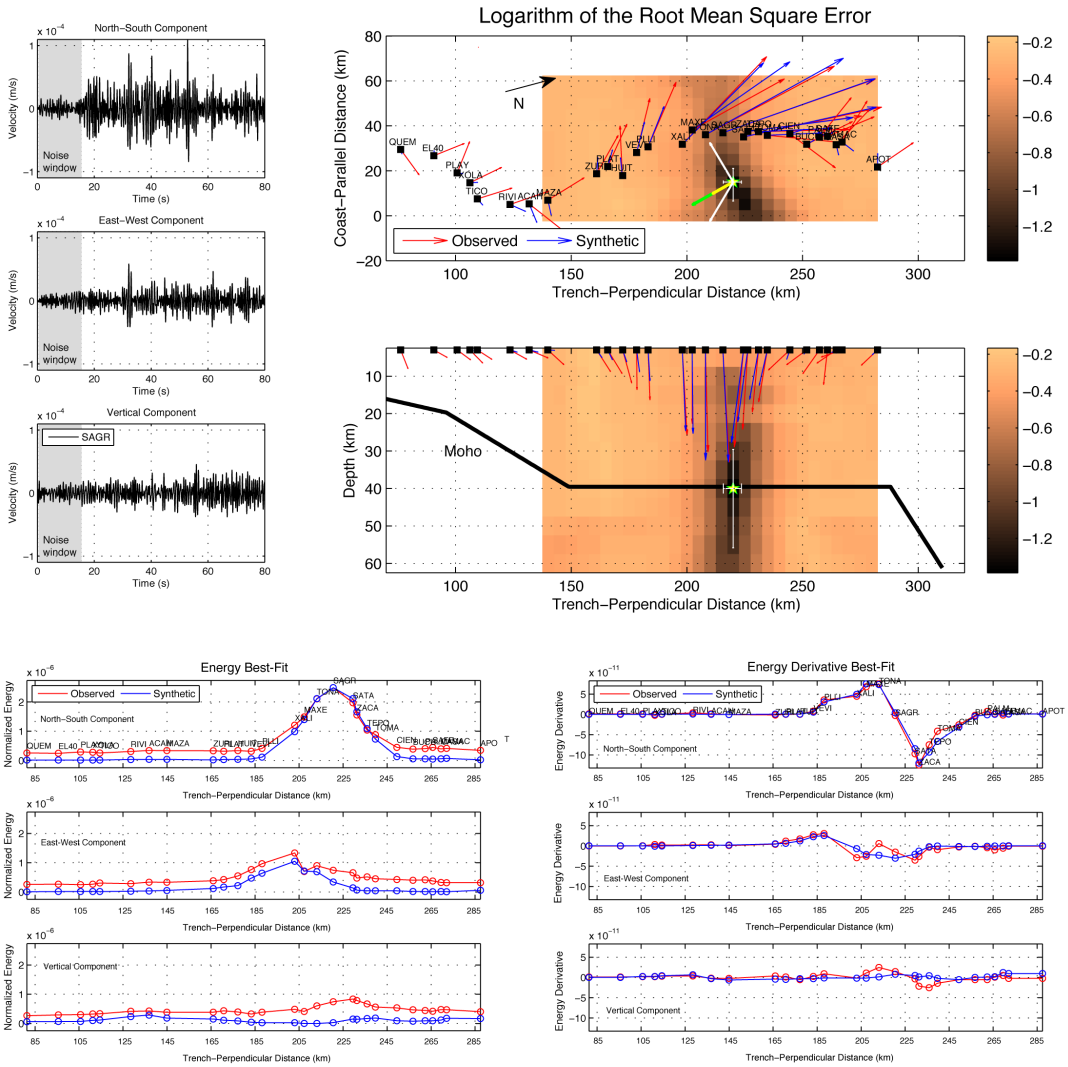

Figure A2 (continue) Same as the previous figure but for SNR = 2.5. Compare with Figure 6 (left column) of the main text.

Signal to Noise Ratio Equal 1.5

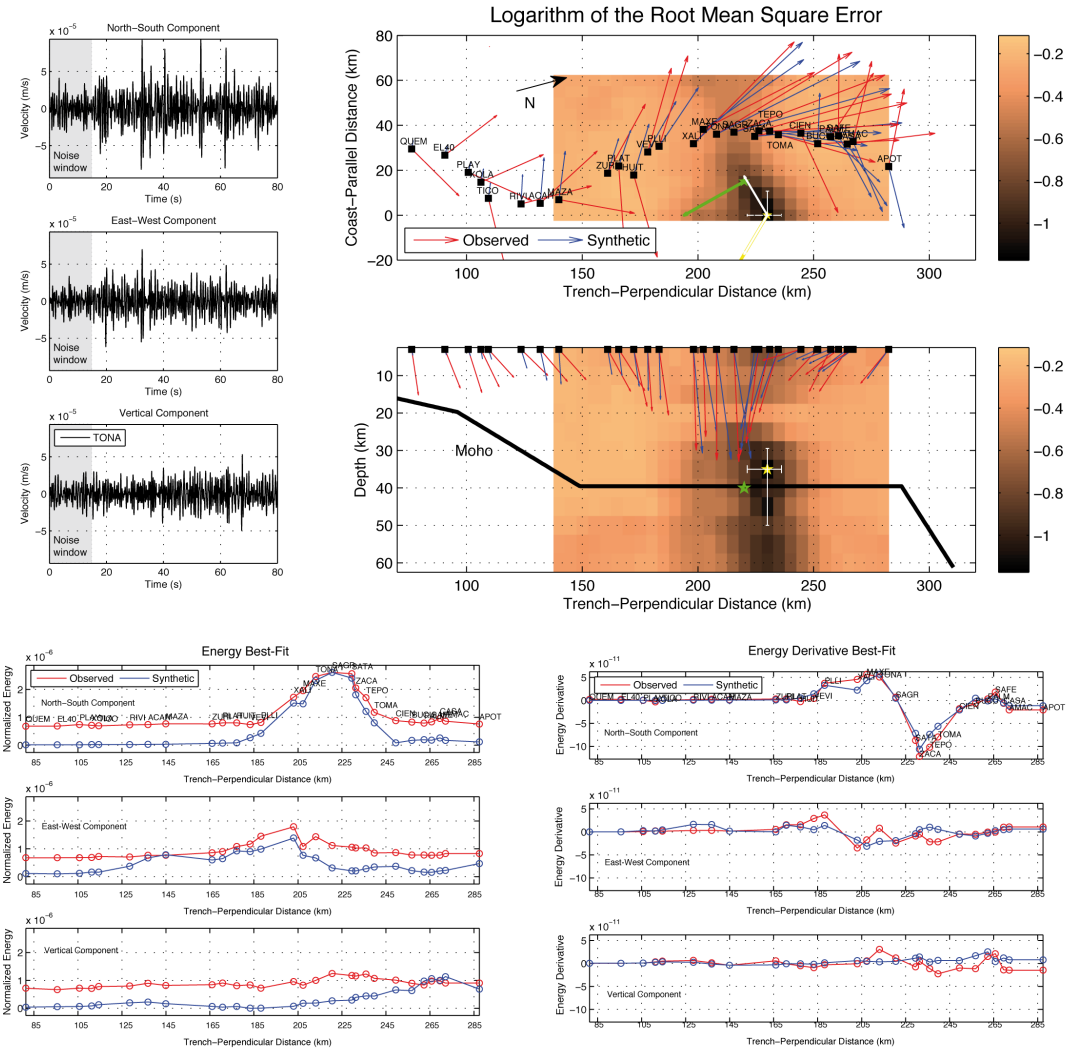

Figure A2 (continue) Same as the previous figure but for SNR = 1.5. Compare with Figure 6 (left column) of the main text.

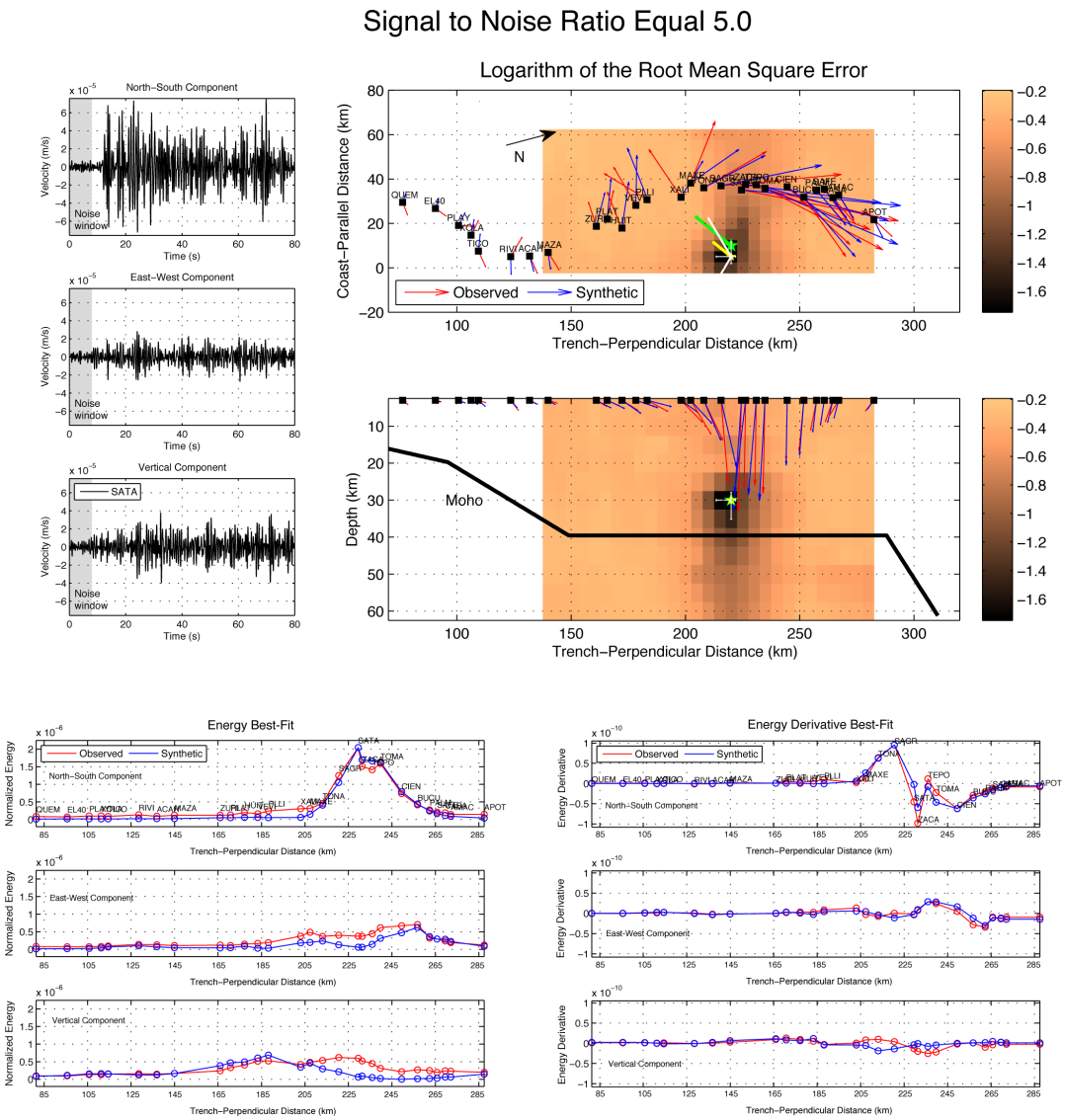

Figure A3 Same as Figure A2 but for a tremor source 30 km depth with different rake angle, and SNR = 5.0. Compare with Figure 6 (right column) of the main text.

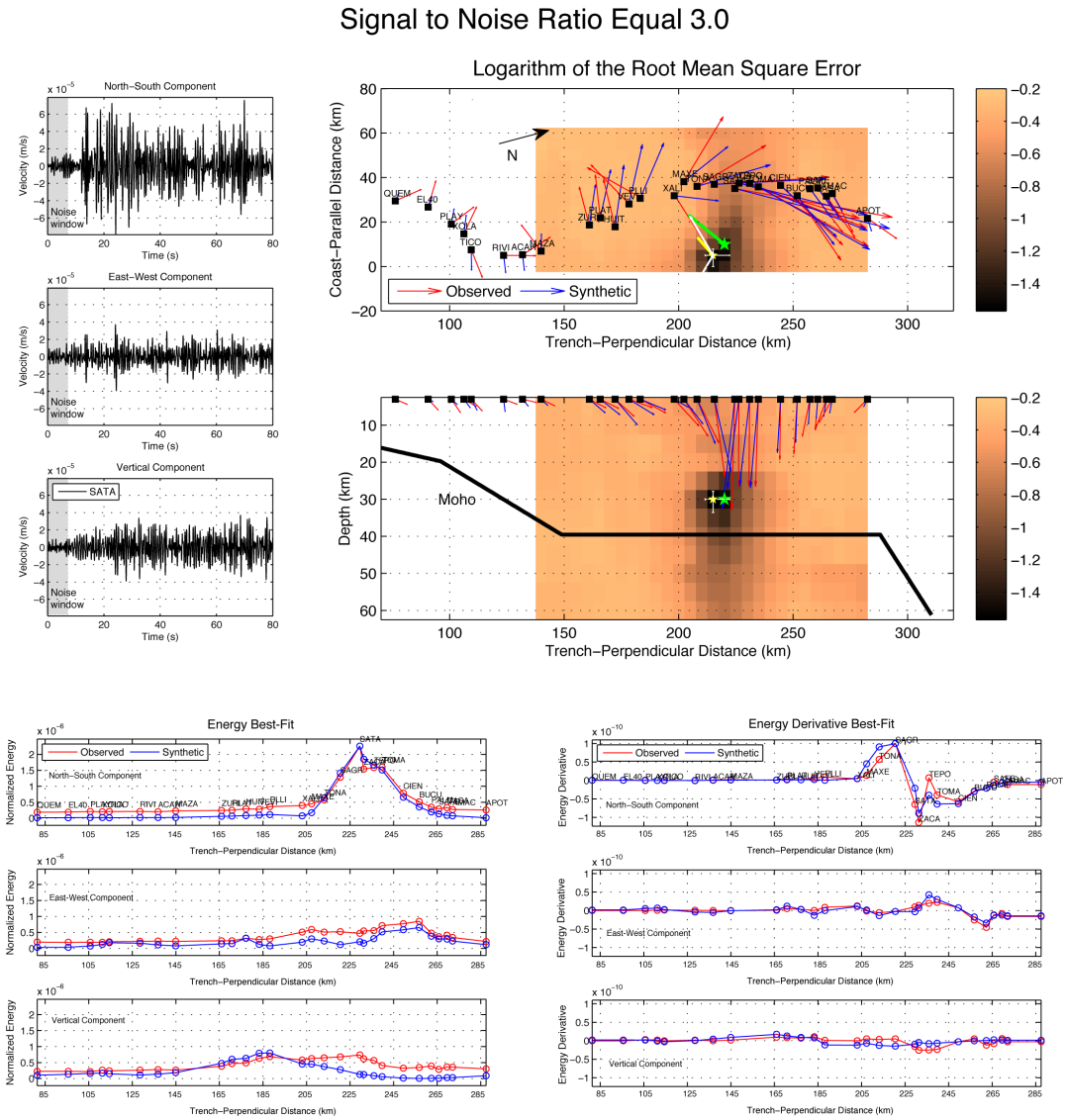

Figure A3 (continue) Same as the previous figure but for SNR = 3.0. Compare with Figure 6 (right column) of the main text.

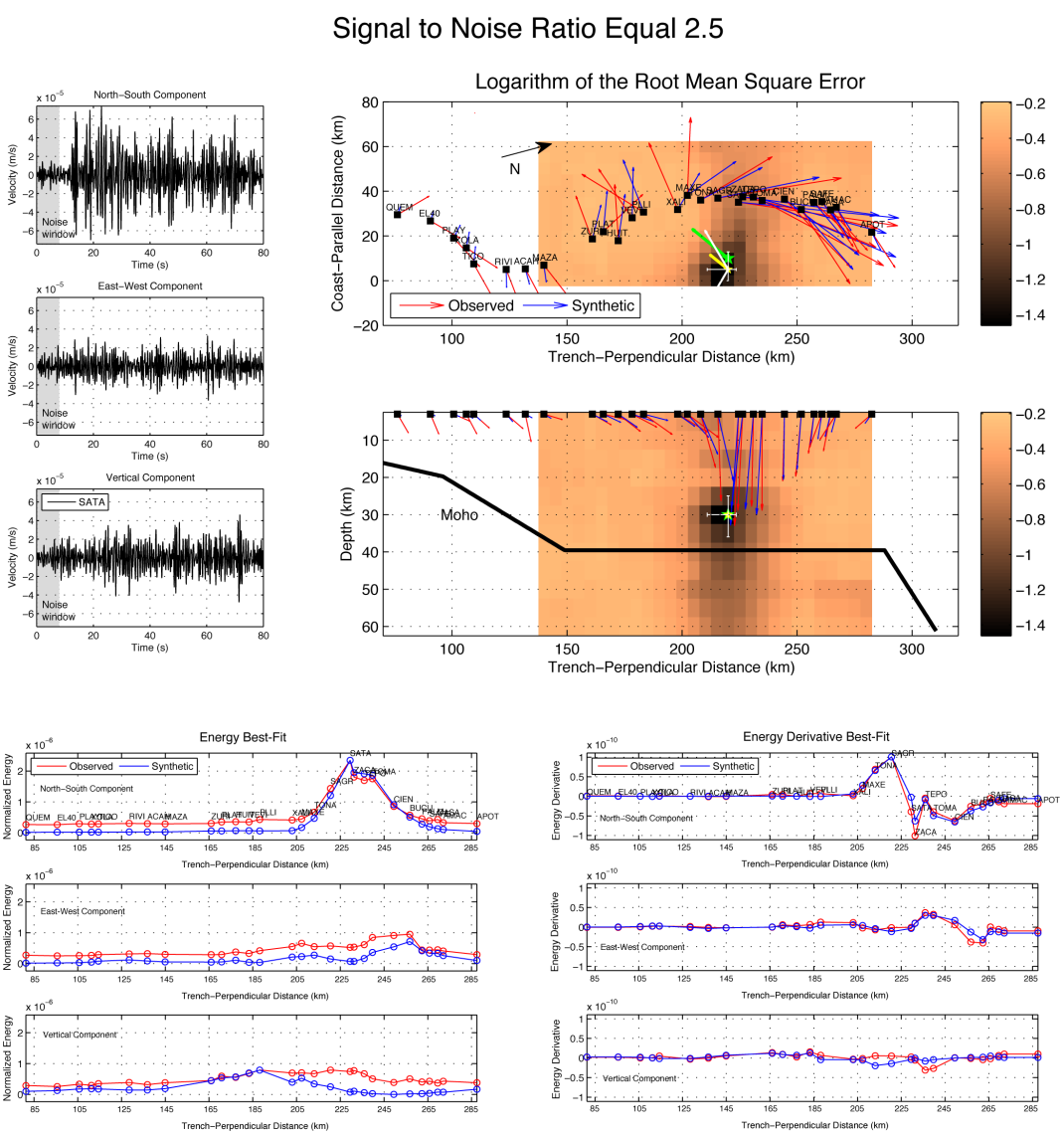

Figure A3 (continue) Same as the previous figure but for SNR = 2.5. Compare with Figure 6 (right column) of the main text.

Signal to Noise Ratio Equal 1.5

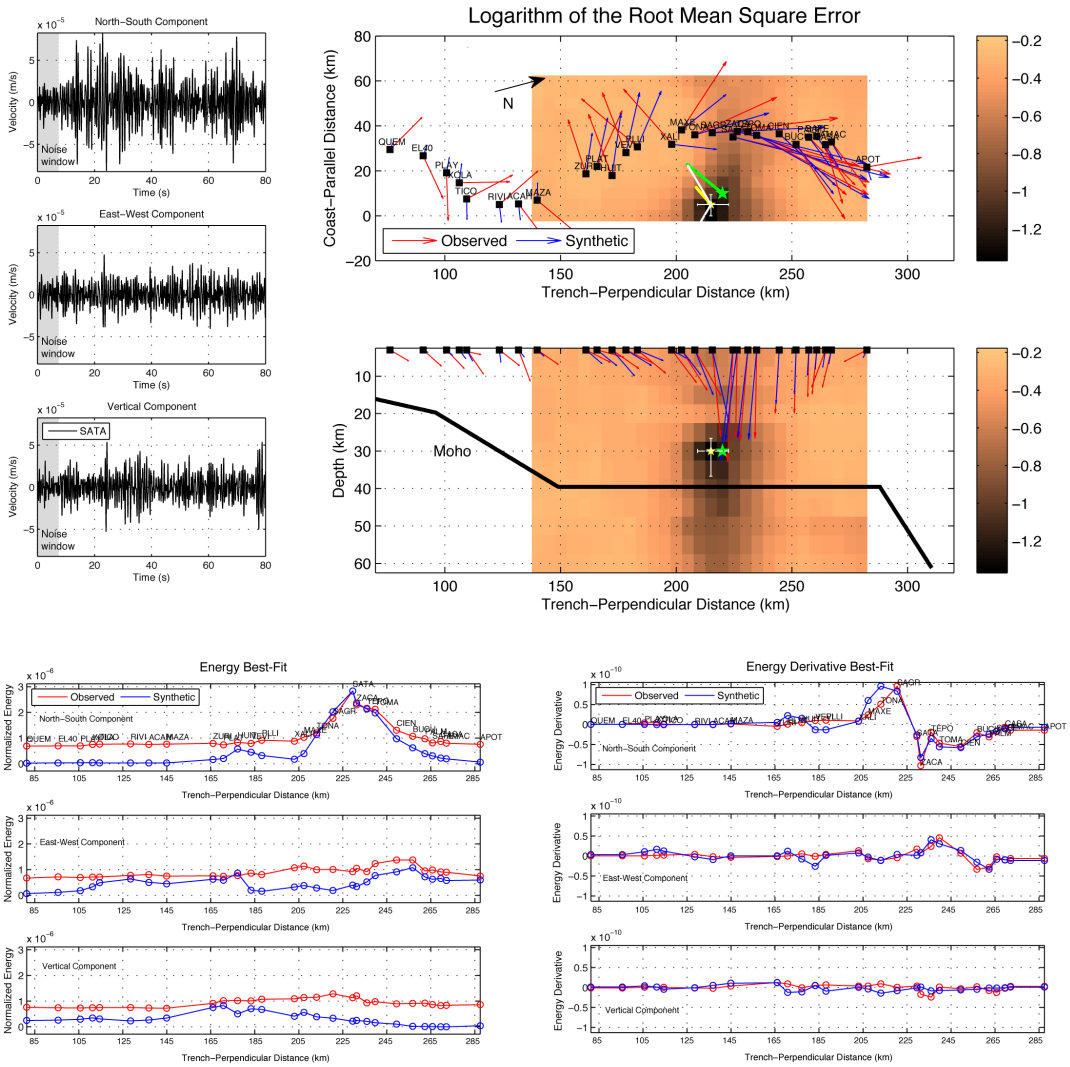

Figure A3 (continue) Same as the previous figure but for SNR = 1.5. Compare with Figure 6 (right column) of the main text.

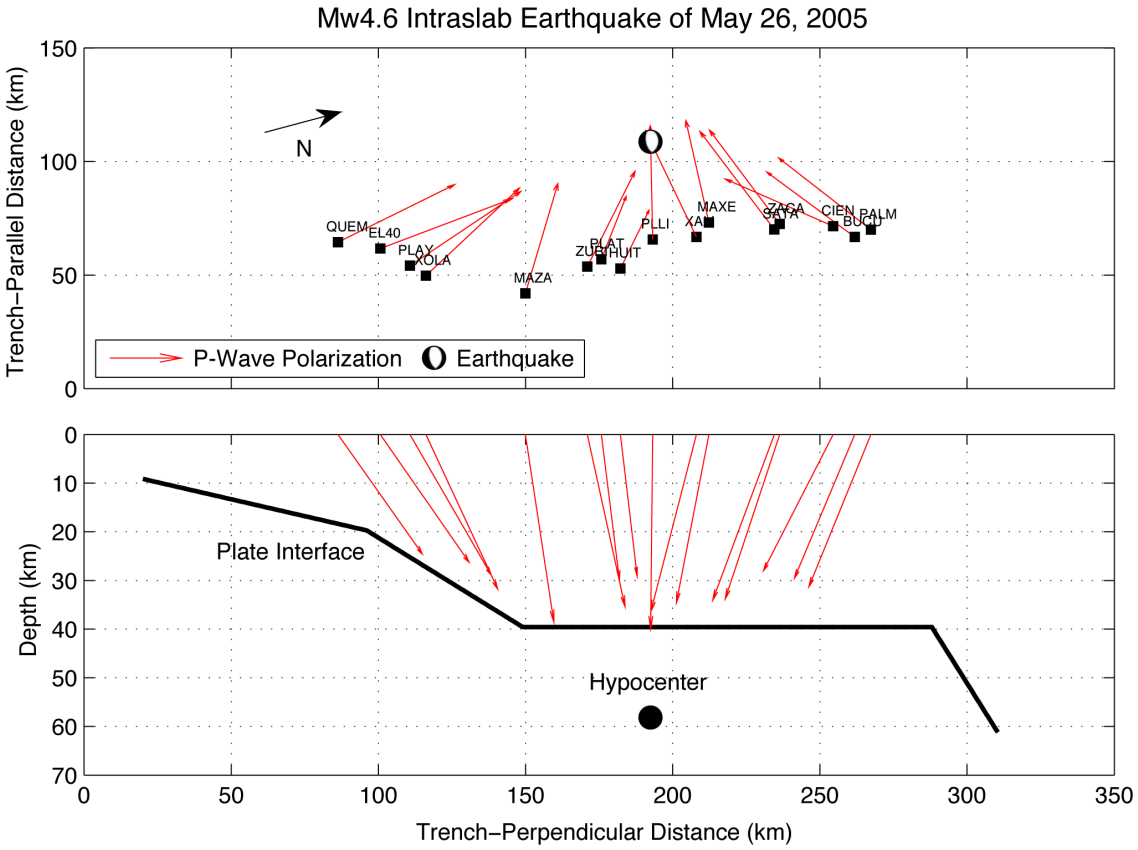

Figure A4 Polarization directions of the band-pass filtered P-wave (1 – 2 Hz) of an earthquake Mw4.5 occurred on May 26, 2005 that was registered in the same station array used to locate tremors. The polarization vectors were determined applying the same technique used by TREP to compute the corresponding observable in the inversions (see Section 2.1 of the main text). This figure shows that path and site effects are negligible in the frequency band considered in the present work to study the NVT sources. Location and mechanism of the earthquake were determined by Pacheco and Singh (2010).

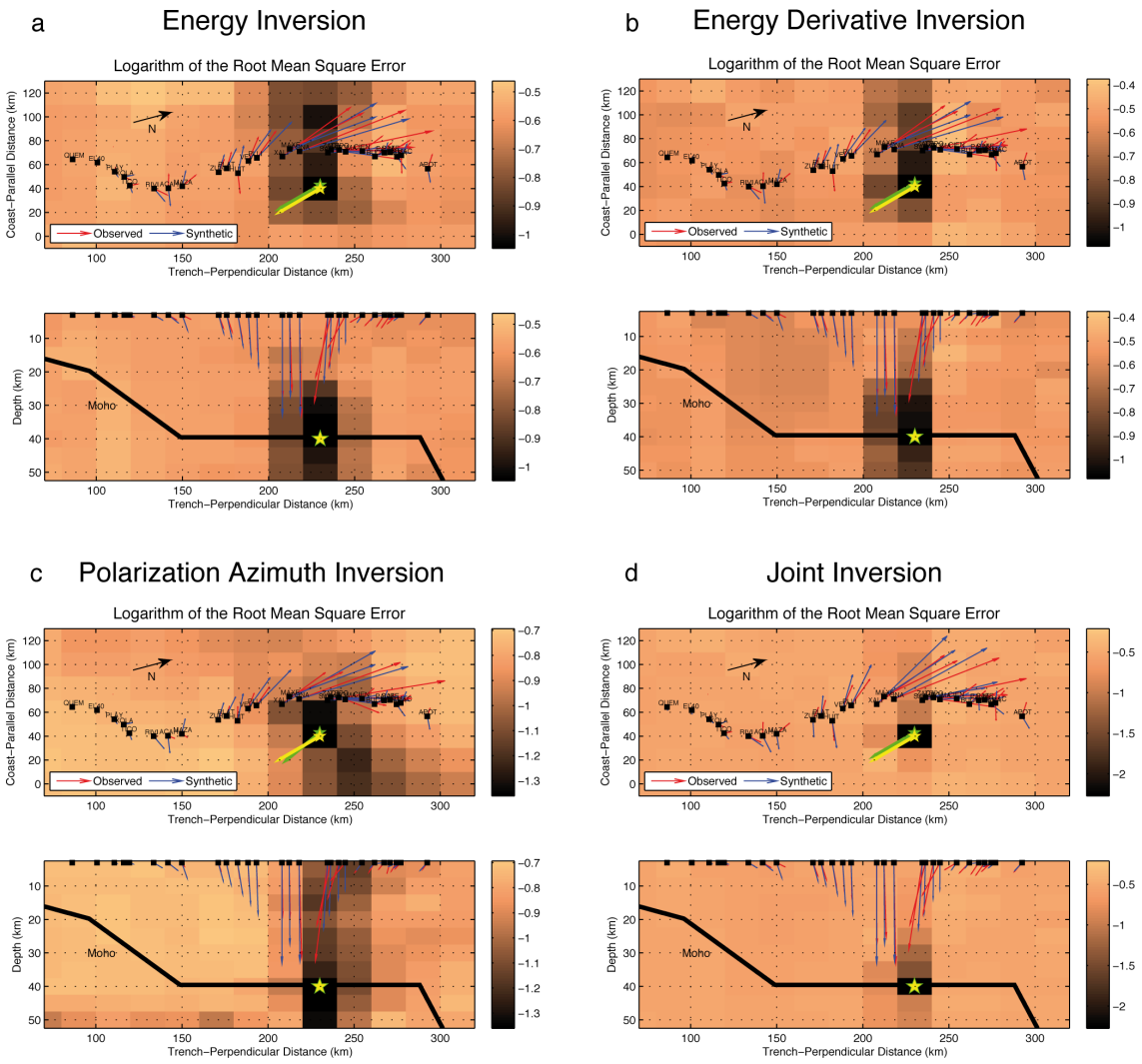

Figure A5 Synthetic inversions for the same tremor-like event illustrating the benefits of combining the three observables (i.e., the energy distribution, the energy derivative and the polarization azimuth) to resolve the tremor source. Red and blue arrows show the observed and synthetic particle motion polarization directions, while the background colors show horizontal and vertical cross-sections of cost function Q through the best hypocenter location (yellow stars). The source target solution is represented with green symbols (location and rake angle). (a) Results from the inversion of the energy alone; (b) results from the inversion of the energy derivative alone; (c) results from the inversion of the polarization azimuth alone; and (d) results from the joint inversion of the three observables.